To the Graduate Council:

I am submitting herewith a thesis written by Girish Gvalani entitled "Software tools for 3-D PET Imaging: Design and Development". I have examined the final copy of this thesis for form and content and recommend that it be accepted in partial fulfillment of the requirements for the degree of Master of Science, with a major in Computer Science.

Jens Gregor, Major Professor

We have read this thesis

and recommend it acceptance:

Brad Vander Zanden

Gary Bronson

Accepted for the Council:

Associate Vice Chancellor and

Dean of The Graduate School

SOFTWARE TOOLS FOR 3-D PET IMAGING: DESIGN AND DEVELOPMENT

A Thesis

Presented for the

Master of Science

Degree

The University of Tennessee, Knoxville

Girish Gvalani

August 1999

ACKNOWLEDGMENTS

There are many people to whom I am grateful for making my time at the University of Tennessee so rewarding. I am particularly thankful to my thesis committee, Jens Gregor, Brad Vander Zanden, and Gary Smith for their support and encouragement. John Ollinger of Washington University, St. Louis, not only provided his source code for scatter correction but also financed my trip to St. Louis so that he could help me better understand his code and modify it for our PET system.

There are a number of other people whose assistance should be recognized. I would like to thank Hedley Bond for the innumerable pieces of code he has written, debugged, and helped me write. Without his help I would never have been able to decipher the arcane mysteries of CTI's software or its equipment. I also wish to thank Desmond Longford, for his guidance and help in doing phantom scans at UT Medical Canter, Shannon Campbell for helping me design all my presentations and his unerring advice on life, Macintosh upgrades, and everything, Kathryn Hunter for her help in setting up the scanning protocols, and Doug Adams of CTI-PET systems, Knoxville, for letting us borrow his phantom for our studies.

Lastly, the greatest debt is owed to my wife, Anju, who stood by me through these two years with patience, good humor, and love. I promise to do the same for her when she begins the next phase of her educational career.

Abstract

This thesis describes the design and development of PET image reconstruction tools within the framework of an easy to use graphical user interface (GUI). The components of this software include image conversion codes, data correction, and codes for image reconstruction and registration of image volumes.

The data correction codes compensate for phenomena such as Compton scatter, random coincidence events, attenuation, and detector efficiency in PET sinograms. Normally, scatter and randoms correction techniques do not improve image quality much for two-dimensional images. However, since nearly 50% of three-dimensional PET sinogram data is noise from these sources, data correction to compensate for these phenomena must be done to achieve reasonable image quality for 3D PET image reconstruction.

The image reconstruction algorithms implemented include Fourier rebinning (FORE) and filtered backprojection (FBP). Filtered backprojection is implemented as a 2D reconstruction method and FORE as a 3D reconstruction application which rebins 3D data into 2D data sets and then uses the filtered back projection method to reconstruct the images from sinograms.

Image registration is the process by which images of different modalities or subjects can be conformed to a common coordinate system so that they can be compared to provide complementary information as in PET and MRI or CT studies.

The graphical user interface (GUI) which wraps around all these modules, presents a cohesive, and easy-to-use framework for any application environment. It has been specifically designed in C++ using the AMULET libraries, for a clinical setting. The interface is user-friendly and provides control over all useful parameters for image conversion, correction, reconstruction, and visualization.

TABLE OF CONTENTS

	CHAPTER	PAGE
1	Introduction	1
	Goal	1
	Scatter Correction	2
	Image Reconstruction	3
	Registration	3
	Data Conversion	4
	Graphical Interface	4
2	Scatter Correction	6
	Measurement Model	6
	Photon Scatter: Background and Relevance to PET	7
	Scatter Models	9
	Klein-Nishina Scatter Correction Algorithm	
	Geometry and Algorithm	10
	Incidence Calculation Process	12
	Final Scatter Formula	16
	Ollinger Model Assumptions	17
	Ollinger Model Implementation	18

	Experiment	22
	Results	22
3	Image Reconstruction	27
	Direct Fourier Methods	27
	Radon Transform	27
	Back-Projection Operator	29
	Projection Theorem	30
	Filtered Backprojection	30
	Three-Dimensional Image Reconstruction	33
	CTI PET 3-D Data Format	33
	3-D Image Reconstruction	37
	Exact Rebinning method for 3-D image reconstruction	38
	Approximate Rebinning algorithm	40
	First Order approximation in α : FORE algorithm	40
	Geometrical Interpretation of FORE	42
	FORE Algorithm	43
	Experiment	47
4	Image Registration	50
	Automated Image Registration	50

	Synopsis of the programs	52
	Description of the **.air** file	53
	Homogenous Coordinates	54
	Spatial Transformation Models	56
	Experimental Results	57
5	Conclusion	59
	Bibliography	62
	Vita	66

LIST OF FIGURES

FIGURE	CAPTION	PAGE
1	Central GUI to select functions to perform on data	5
2	Compton Effect – energy loss versus photon scatter angle	8
3	Geometry of Scatter in PET scanner	11
4	Parameters for calculating incident flux on voxel	13
5	Divergence of photons during propagation through voxel	15
6	Scatter correction flowchart	20
7	Single scatter correction flowchart	21
8	Experimental setup to study scatter correction	23
9	Scatter-corrected vs. uncorrected data – direct plane 11	24
10	Scatter-corrected vs. uncorrected data – cross plane 11	25
11	Projection imaging geometry	28
12	Filtering sinogram before 2-D backprojection flowchart	31
13	2D Backprojection of filtered sinogram	32
14	2D PET image data acquisition - experimental setup.	34
15	3D PET image data acquisition - experimental setup.	35
16	CTI PET 3D data format ECAT 7.1	36
17	Principle of rebinning algorithms	39

18	Geometry of cylindrical PET scanner	41
19A	Geometric interpretation of Fourier rebinning	44
19B	Dependence of rebinning on ω-k region	44
20	FORE algorithm flowchart	45
21	Rebinning algorithm flowchart	46
22	FORE vs 2-D FBP reconstruction	49
23	GUI for setting up AIR parameters	58
24	GUI for displaying coregistered image sets	58

CHAPTER 1

Introduction

Goal

PET scanning is the process by which regions within a body may be imaged. This is done by injecting the patient with a metabolically active radioactive substance which decays and emits positrons within the body. Each positron quickly annihilates with an electron to produce two gamma-rays that are emitted at an angle of 180° with respect to one another. Photon detectors arranged in rings about the patient's body detect coincident photons thus measuring count rates of photon emission.

PET image data is collected in the form of projections. Each projection is a collection of data bins, each of which is a line integral sum along a straight path through the object being imaged. Upon detection, a measurement representing the line integral of the absorption distribution along each path is obtained. This collection of line integrals for each angle between 0 and π radians is known as a sinogram.

The goal of this project has been to create various software components essential to the data conversion, correction, and reconstruction of 2D and 3D PET images. The GUI created supplies a plug-as-needed architecture for these modules. The data conversion modules are required to convert among CTI System's proprietary ECAT 6.5 and 7.1 data formats, and raw data. The correction module is for Compton Scatter

correction (Russell, 1984) as addressed in Chapter 2. The reconstruction modules are of two types: 2D reconstruction which uses only direct axial plane data, and 3D reconstruction (Defrise, 1997) which uses direct and oblique planes to provide a direct three dimensional reconstruction. Experimental work has also been done with phantoms on the ECAT 921 CTI PET scanner at the University of Tennessee Medical Center, Department of Radiology. This work is used to study the effectiveness of the computational models.

Scatter Correction

As positrons annihilate each other to generate 511 keV photons, these rays get scattered by internal structures in the patient body before reaching the detector crystals of the scanner. The scattering angle of these rays can be calculated by a process known as the Compton Effect (Russell,1984), which effectively says that the photons lose energy as a function of their scatter angle. By measuring the energy loss the true unscattered events can be windowed at every detector thus forming a clean image during reconstruction. Several algorithms may be used to correct for scatter but the Klein-Nishina model as formulated by Dr. John Ollinger,Washington University, St. Louis (Ollinger, 1996) seems to provide a true analytical picture of the process.

Image Reconstruction

The 2D reconstruction technique used is standard 2D filtered backprojection (FBP) (Jain 1989). The analytical 3D technique used is the Fourier rebinning algorithm (FORE) (Defrise Michael 1997), which rebins oblique plane data into 2D direct planes in Fourier space based on linear interpolation. This technique has been proven to provide equivalent quality to the 3D reprojection (3DRP) technique while avoiding the pitfalls such as noise propagation of other multi-slice rebinning techniques.

Registration

Registration of two image sets is the process by which one image is designated as the reference image and the other image is transformed by a variety of linear and non-linear transformations to match key features to those in the reference image. The purpose of this process is to compare images acquired in different modes, such as PET and MRI, in order to determine complementary information. The Automated Image Registration (AIR) package is primarily designed to solve several different registration problems that arise in tomographic data sets (Woods RP 1992; Woods RP 1993; Woods RP 1998A; Woods RP 1998B). Once the registration parameters are known, the AIR package allows the data to be resampled to generate a final image using one of many interpolation models, such as, nearest neighbor, trilinear, windowed sinc, etc.

Data Conversion

The data acquired by the scanner is in CTI's proprietary ECAT 6.5 and 7.1 formats. Code modules (Bond, 1998) used to convert between these formats and raw data were also incorporated into the GUI as utilities.

Graphical Interface

A graphical interface was implemented in C++/C with use of the AMULET Toolkit (Myers, 1997) to serve as a user-friendly means to access and execute all codes. The GUI system was designed as a central graphical interface (Figure 1) whose buttons invoked different functions, such as scatter correction, image reconstruction, and registration. Each function is represented as a series of GUI interfaces with each interface calling its child to perform the next task in the process of performing the function. Each interface collects information from the user relevant to the processing of that level's task. After collecting the information, the kernel behind the interface performs its task and then the interface invokes its child interface which collects information it needs to perform the next task in the chain.

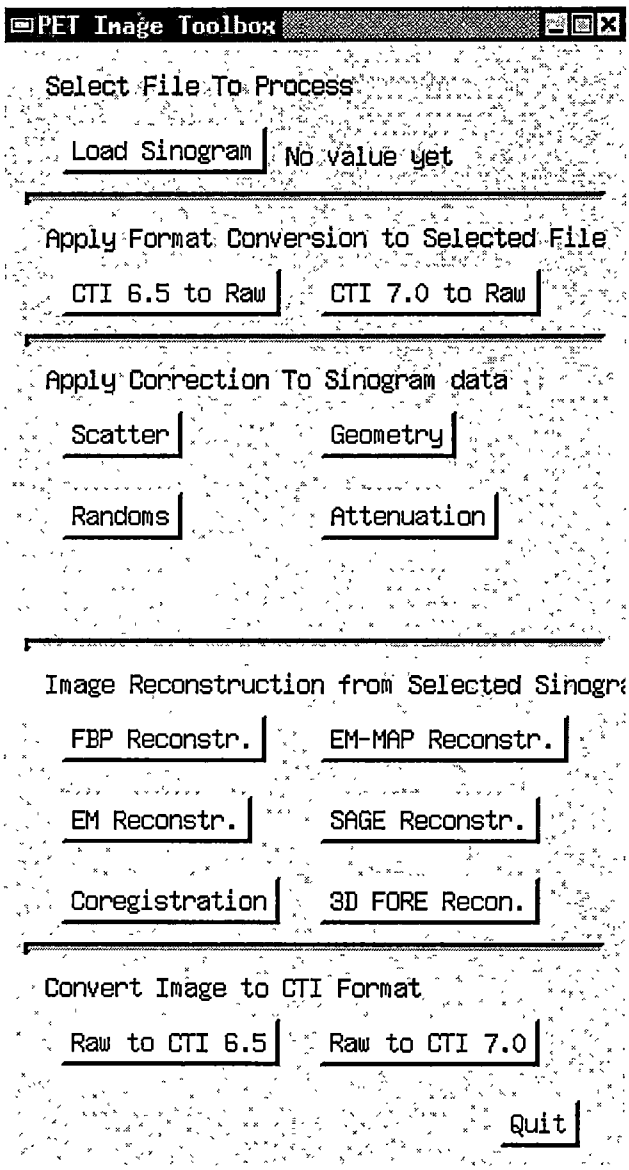


Figure 1: Central GUI to select functions to perform on sinogram data files

CHAPTER 2

Scatter Correction

Measurement Model

Acquired PET scanner data can be modeled as a set of independent Poisson random variables x_i with mean $\hat{x}_i$ equal to the sum of three components: true coincidences $\hat{e}_i$, randoms $\hat{r}_i$, and scatter $\hat{s}_i$ (Mumcuoglu, 1996).

$$\hat{x}_i = E(x_i) = \hat{e}_i(\lambda) + \hat{s}_i + \hat{r}_i$$
$$\hat{e}_i(\lambda) = \sum_j p_{ij}\lambda_j$$

where p_{ij} is the probability of detector pair i recording emissions from pixel j. The p_{ij} probabilities can be conveniently expressed in matrix form as:

$$P = P_{Detectors}P_{Attenuation}P_{Geometry}$$

- $P_{Detectors}$ is a diagonal matrix of scaling factors for detector efficiency (dead time)
- $P_{Attenuation}$ is a diagonal matrix of scaling factors for attenuation.
- $P_{Geometric}$ contains geometric detection probability values.

This allows us to calculate true coincidences $\hat{e}_i$ using known algorithms to compute $\hat{s}_i$ and $\hat{r}_i$. Once $\hat{e}_i$ has been computed from measured data, it may be used to reconstruct true images using a variety of methods.

Photon Scatter: Background and Relevance to PET

According to modern physics, light behaves both as a particle and as a wave. Sir Arthur Compton carried out one of the crucial experiments proving its particle nature in 1922 (Russell, 1984). Compton sent X-rays through thin metallic foils and discovered that the scattered X-rays came out on the other side with one of two wavelengths. One wavelength was that of the original X-ray. The other was longer and seemed to be a function of the angle of scatter of the X-ray from its original path (Figure 2). The formula defining this dependence works out to be:

$$\lambda_S - \lambda_0 = \frac{h}{mc}(1 - \cos\theta)$$

where λ_0 is the wavelength of the incident X-rays and λ_S that of the scattered X-rays and m is the electron mass. This result comes about due to the fact that the momentum of the scattered photon must be conserved even if its energy is not. Since the wavelength of a photon is directly related to its energy by Planck's formula, $E = \frac{hc}{\lambda}$, the energy of the scattered photon is decreased from that of the incident photon as a function of the angle of scatter. This change in energy is the quality used in general to detect scattered photons in PET data. The Klein-Nishina result (Evans, 1955) uses Compton's scatter formula to compute the probability that a photon scattered at any given point will scatter at a given angle. This probability when multiplied by the total number of photons that can scatter at

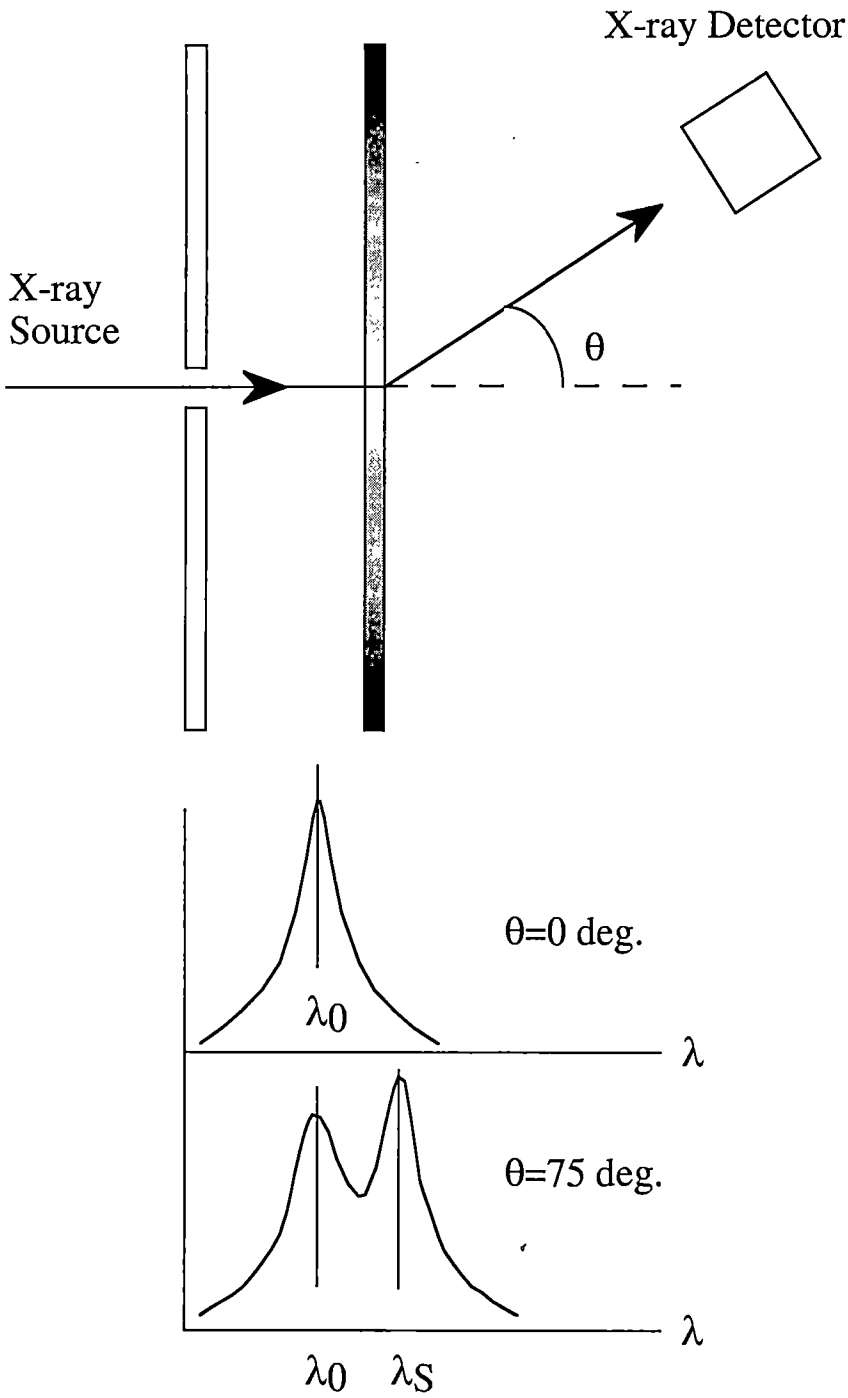


Figure 2 : The Compton effect demonstrates the correlation between energy loss and scatter angle of photons.

a given point, gives the total number of photons that scatter towards a particular detector from a given point.

Scatter Models

Once the measurement model and the process of scatter is known, the next step is to estimate $\hat{s}_i$, the mean scatter rate. There are two main methods in computing the scatter fraction: model based and empirical methods. Model based methods tend to examine the actual process of scatter and calculate the scatter fraction based on the process. Other scatter methods such as Grootonk and Shao's dual energy window correction (Grootonk, 1991; Shao, 1994) make assumptions about the distribution of scatter at high and low energies. Bergstrom's method (Bergstrom, 1983) of treating scatter as an integral transformation of the emission data does not take into account data originating from outside the field of view, and relies on phantoms which do not adequately mimic the human anatomy. Karp (Karp, 1990) and Cherry and Huang (Cherry, Huang, 1995) use fitted functions such as second-order polynomials and Gaussian functions to interpolate from scatter in regions of the sinogram that do not sample the image. The difficulty with these methods is that the shape of the scatter distribution is assumed. This is not appropriate especially for scans in large inhomogeneous regions of the body such as the chest. The Klein-Nishina method used by Ollinger (Ollinger, 1996) for scatter correction is also the method used by CTI systems in

their scatter-correction software. The main advantage to using this method is that the actual scatter process gets modeled as faithfully as possible so as to get an accurate measure of scatter, without assuming the geometry of the object being imaged. The Klein –Nishina method is not spatially invariant as it accounts for scatter locally in each region of interest.

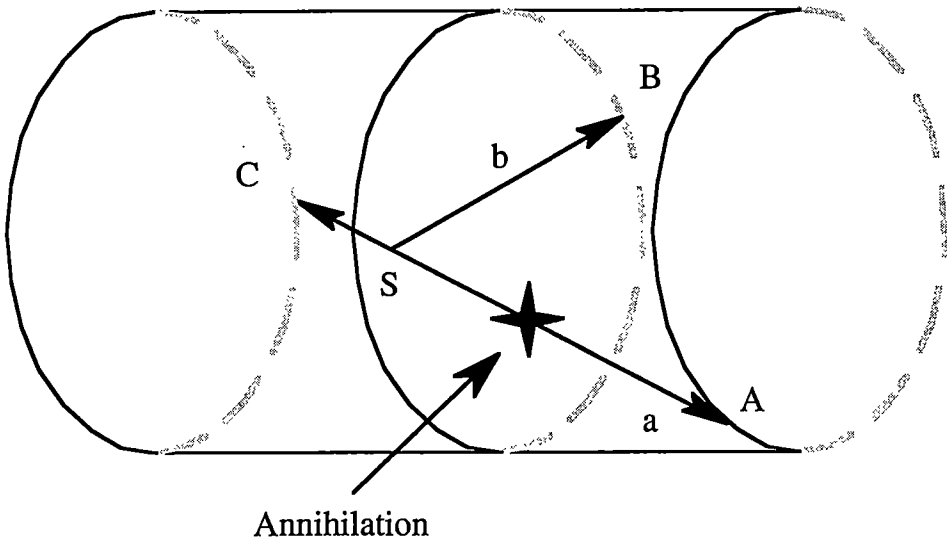
Geometry and Algorithm

The paths of the annihilation photons for a single scatter are shown in figure 3. The unscattered photon's path is from the point of annihilation to the detector at A. The scattered photon of the pair is scattered at S towards the detector at B. If this photon were not scattered it would intersect the detector surface at C. The scattered coincidence is positioned along the line of response AB of length L.

The idea behind Ollinger's algorithm for estimating the number of scattered coincidences along lines of response such as AB is as follows:

1: For each scattering point S along AC, the number of photons travelling along **b** is calculated, for which corresponding photons have been detected at A. This is the incidence calculation.

2: From the number obtained by the incidence calculation, the total number of photons scattered can be calculated from the linear attenuation coefficient given by transmission images.



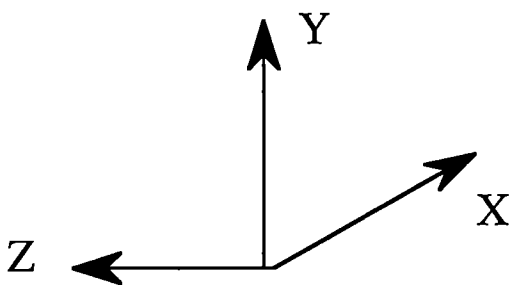


Figure 3 : The paths of the annihilation photons for a single scatter are shown here. The unscattered photon's path is from the point of annihilation to the detector at A. The scattered photon of the pair is scattered at S towards the detector at B.

(Adapted from (Ollinger, 1996))

3: Then the Klein-Nishina formula is used to calculate the fraction of photons scattered towards B.

4: Finally the attenuation along line SB is calculated (Figure 3).

Similarly calculate this series for all necessary lines of response AB in data set.

Incidence Calculation Process: (Figure 4)

To compute the number of incidence photons that can be scattered, the incidence flux per voxel is calculated and then sum over all voxels. In Figure 4 the cross-section of the imaging volume is divided into a matrix of l*d voxels in the rotated l-d coordinate system. The number of photons incident at voxel S that could result in scattered coincidences is given by:

$$N_{sd}(\theta,\psi) = \frac{1}{N_\theta}\sum_{l=0}^{s}\eta_{ls\psi}\left(\int_{z_{min}}^{z_{max}}\lambda_{ld\theta}(z)dz\prod_{i=0}^{l}\beta_{id\theta\psi}\right)$$

The method for calculating the total number of photons incident at each point that could be scattered is as follows:

1: Rotate emission volume by transverse angle θ. This gives array $\lambda_{ld\theta}(z)$ of the emission intensities in the rotated coordinate system. The rotation is done to calculate the scatter distribution at that projection angle. The xy coordinates have been replaced by the l-d coordinates in the rotated system.

2: The number of incident photons is recursively calculated along path AS. At each

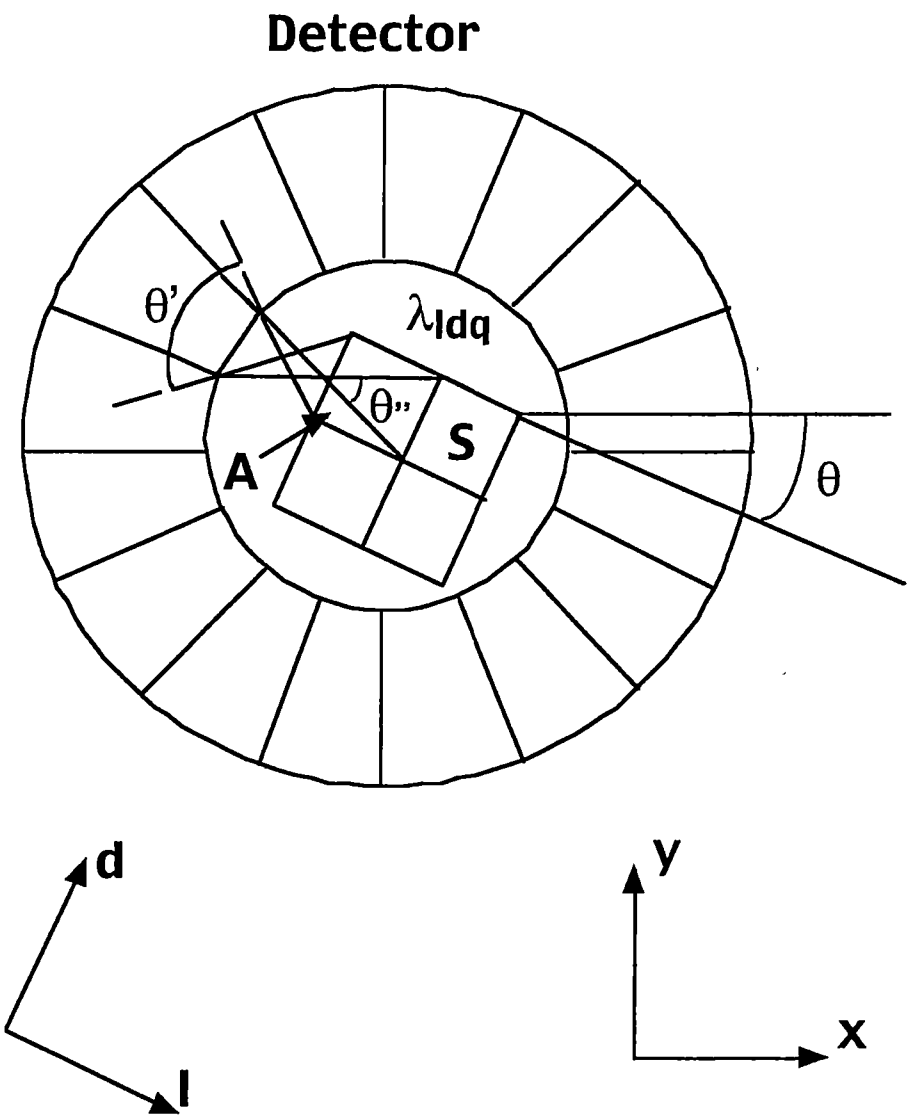


Figure 4 : This figure shows the important parameters related to calculating the incident flux on a voxel that can be scattered.

voxel, the number of photons incident on the voxel is added to the product of the following terms:

a: Emission Intensity: Integral over the voxel. The beam of incident photons diverges as it propagates through the subject. So we need to integrate over the divergence in the voxel (Figure 5) :

$$\int_{z_{min}}^{z_{max}} \lambda_{id\theta}(z)dz$$

b: Probability of unscattered photon not interacting in the subject (μ is the attenuation coefficient given by a transmission scan) :

$$\prod_{i=0}^{l} \beta_{id\theta\psi} (= e^{-\mu_{id\theta\psi}\Delta l})$$

c: Probability of unscattered photon impinging on detector of interest.

$$\eta_{ls\psi} = \Omega_u(l)\theta'' / 4\pi\theta'$$

The η factor is simply the fraction of the solid angle subtended by the detector at distance l, $\Omega_u(l)/4\pi$. With reference to figure 4, θ'' is the angle subtended by voxel S on the detector and θ' is the angle subtended by voxel A on the detector. Since the divergence of the photon beam is accounted for in the XZ plane but not in the parallel geometry configuration of the XY plane, the correction factor for this divergence given by θ''/θ' is multiplied into the η factor. This ratio is the probability that the unscattered

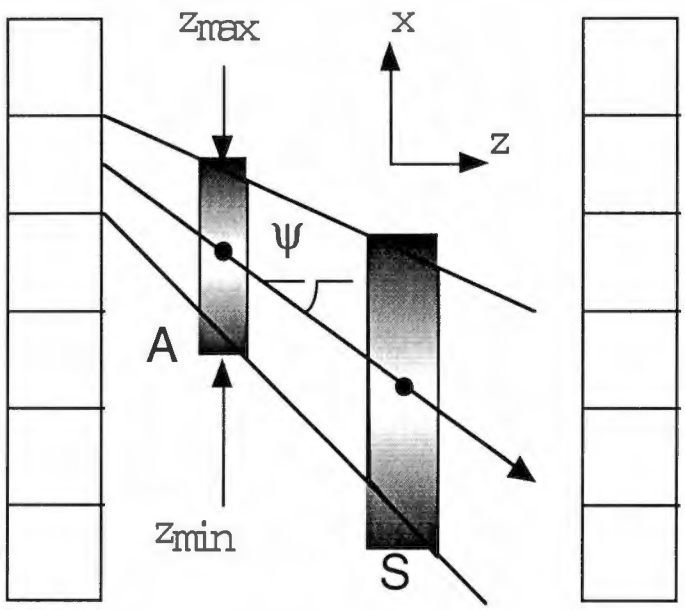


Figure 5 : Since the photon beam diverges as it propagates through the voxel, the divergence has to be taken into account by integration between zmin and zmax to calculate the incident flux $\lambda_{ld\theta}$

photon reaches the detector from a distance l away from the detector.

Final Scatter Formula:

The mean number of scattered events is equal to the product of the incident flux on a voxel that can be scattered given by the equation for $N_{sd}(\theta,\psi)$ and the following terms:

• Probability of a photon being scattered as it propagates through voxel S:

$$1-\beta_{sd\theta\psi}$$

• Probability of a photon being scattered towards detector B – Klein-Nishina formula:

$$P_{KN}(l_2,\upsilon_s)$$

l_2 is the distance between the points of scatter and detection. υ_S is the scatter angle.

• Attenuation of the scattered photon: $\gamma(l_2,\psi,\theta,d,z,E_s)$. First, two tables are constructed; one of attenuation at 511 keV, and the other of $\rho(E_s) = \mu_w(E_s) / \mu_w$ at (511 keV), which is the ratio of the attenuation coefficient of water at energy Es to the attenuation of water at 511 keV. Then the attenuation coefficient at energy E_s can be approximated by $\mu(E_s)=\rho(E_s)\mu(511\text{ keV})$.

$$\gamma(l_2,\psi,\theta,d,z,E_s) = \gamma(l_2,\psi,\theta,d,z,511\text{keV})^{\rho(E_s)}$$

• Probability of photon being detected. Model the energy spectrum as a Gaussian centered at the incident energy of the photon:

$$P_E(E_S)$$

•Finally by summing appropriately, the flux of singly scattered photons along a line of response is given by:

$$\hat{s}_i = \frac{4\pi}{\Omega} \sum_{d=0}^{D_{max}} \sum_{s=A}^{B} P_E(E_S)\gamma P_{KN}(l_2, \vartheta_s)(1-\beta_{sd\theta\psi})N_{sd}$$

Ollinger Model Assumptions

Certain assumptions are made by Ollinger in actually implementing the above scatter fraction computation:

1: Single Scatter Approximation – Assume single not multiple scatter for most scatter events. Monte Carlo studies show 75-80% of scatters are single scatter events.

2: Multiple Scatters – Multiple scatter distribution modeled as an integral transform of the single-scatter distribution.

3: Quantitative Emission Images – Assume emission images to accurately reflect intensity of annihilation process. Iteratively compute scatter distribution from emission image, correct emission image with calculated scatter distribution and re-compute new scatter distribution from corrected image.

4: Quantitative Transmission Images – Assume transmission images accurately reflect narrow-beam linear attenuation coefficient.

5: Detector Efficiency – this is assumed to be the same for scattered as well as true coincidence. Geometric effects are incorporated into single-scatter model – not folded into detector efficiency factor.

6: Energy Resolution – Assume energy resolution to be well modeled as Gaussian, with a variance determined by measured energy resolution.

7: Compton Scatter – Assume this to be dominant interaction. Photoelectric absorption is rare at energies encountered. (Photoelectric absorption is the process by which radiation of a particular wavelength is absorbed by a material target and used to raise the target to a higher energy level. In Compton scatter, the radiation is reflected from the target with no change in the target's atomic or nuclear energy state).

8: Scatter from outside field of view – Assume regions outside sampling region to have same spatial scatter distribution as regions sampled by emission and transmission images.

Ollinger Model Implementation

The trick is to have a computationally feasible algorithm. Three techniques are widely used to make this happen:

1: Extensive use is made of lookup tables to compute equations. This avoids needless recomputation of formulae.

2: All computations are sampled at minimum necessary rate. For example, the sampling rate of the scatter distribution is determined by the resolution of the scatter distribution. This is the reason why sinograms are downsampled before scatter computation, typically by a factor of 2-4 (Figure 6). Once the correction has been computed the sinograms are again upsampled to their original size.

3: Rather than using a fully 3D reconstruction method, the emission volume is approximated by a set of stacked 2D direct planes. The scatter algorithm only uses 2D data to iteratively compute the scatter correction, which it then uses to correct data in all planes in the last step.

Overall Algorithm is implemented as follows: (Figures 6,7)

1. Extract direct plane emission and transmission sinograms.
2. Reconstruct transmission images.
3. For (given number of iterations)
    a. Reconstruct emission images.
    b. Estimate scatter for direct planes.
    c. Correct direct plane sinograms.
4. Reconstruct 2D emission images.

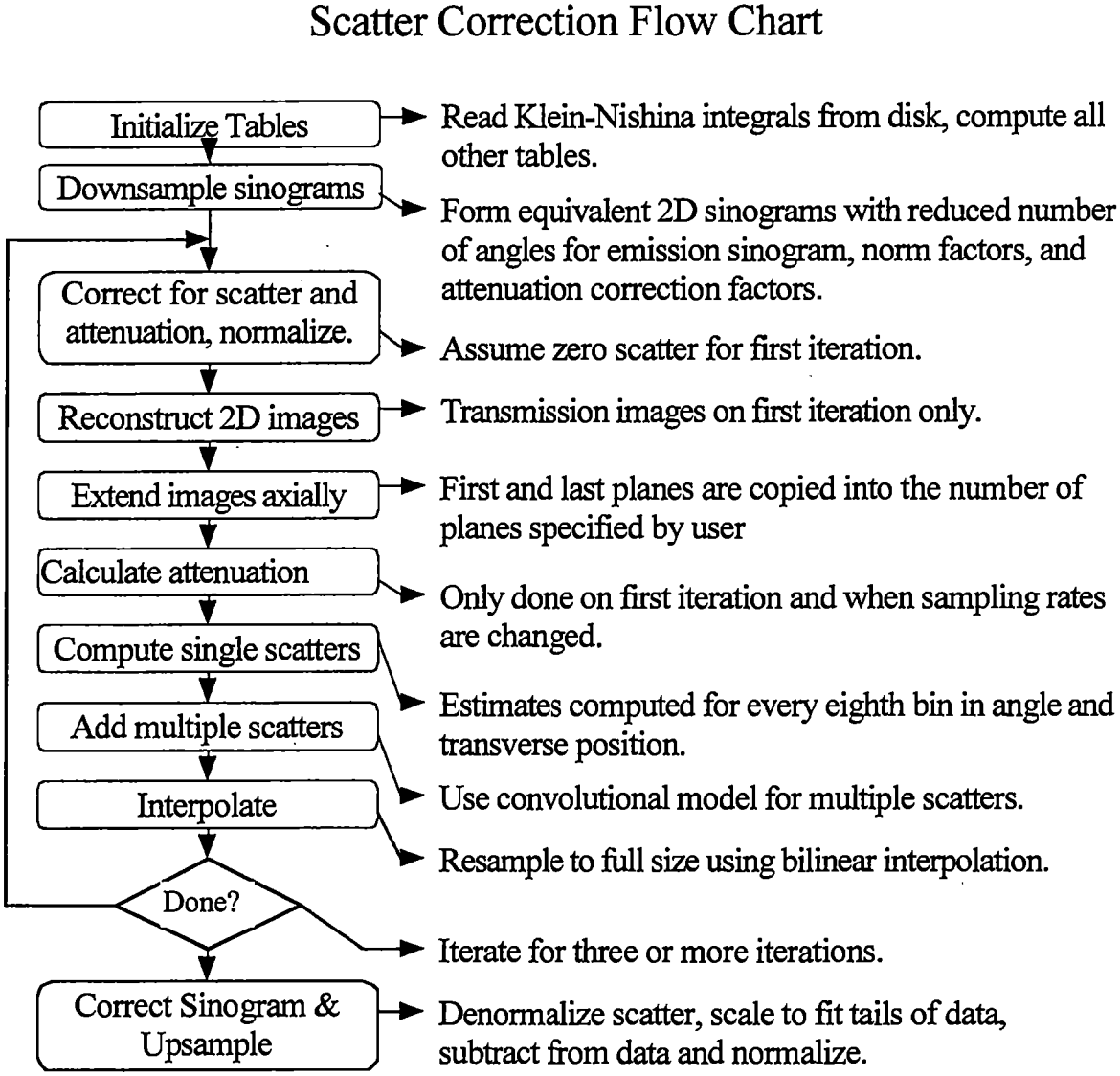


Figure 6: Flowchart for the complete scatter correction algorithm including normalization and scatter correction.(Adapted from (Ollinger, 1996))

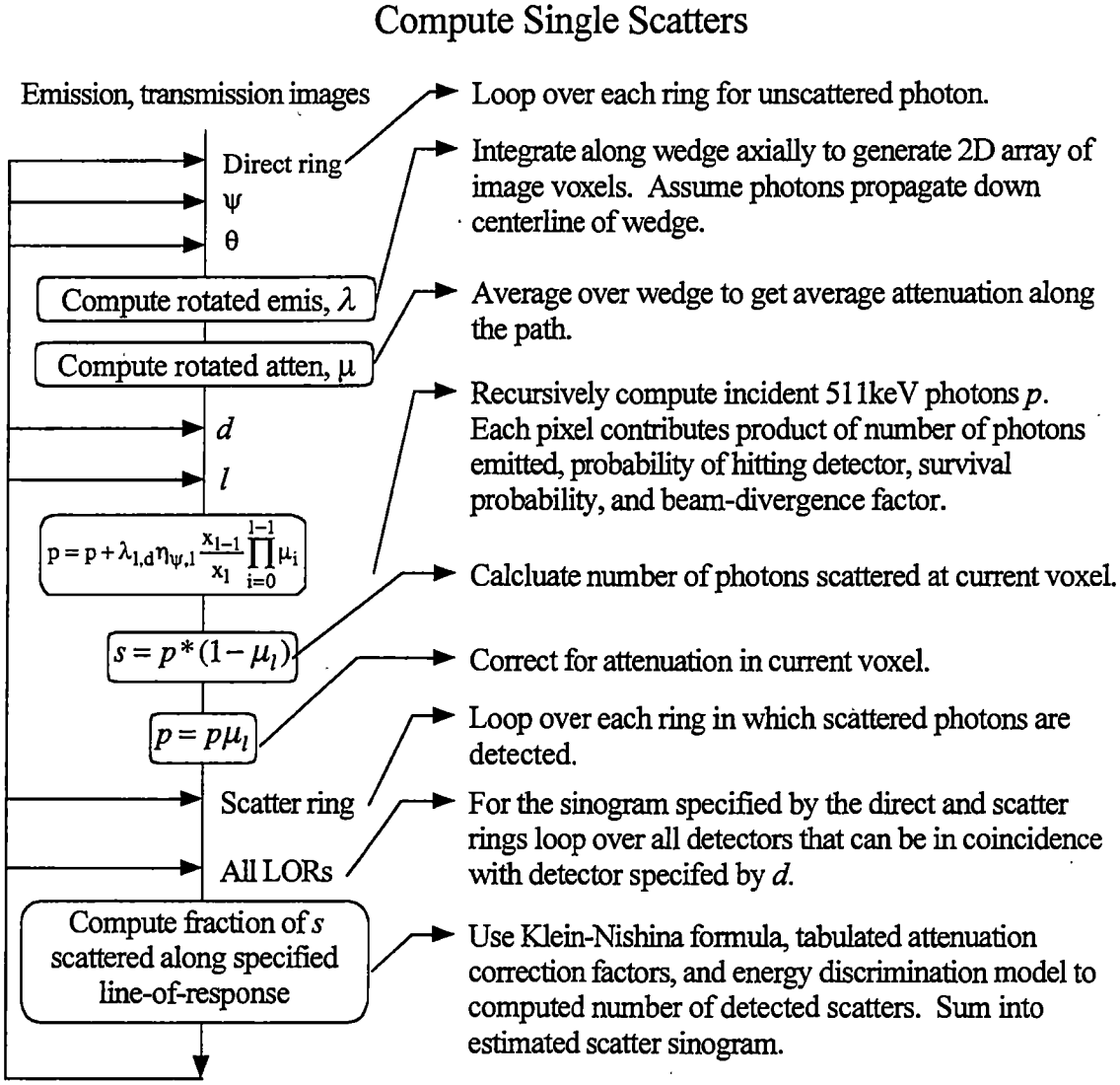


Figure 7: Flowchart for the computation of single scatters. (Adapted from (Ollinger, 1996))

5. Estimate scatter for direct and oblique planes.

6. Correct 3D emission sinograms.

All reconstructions are simple 2D FBP calculations.

Experiment

Two sets of PET scans were acquired using a line source of FDG (fluoro-deoxy glucose) radioactive source with a half life of 117 minutes. The line source was a syringe about 6 mm in diameter and 20 cm in length. The scatter medium was clinically pure de-ionized water at room temperature in a Plexiglas cylinder as shown in Figure 8. The detector electronics measure coincidences within an energy threshold and save the data as sinograms. Each scan series consists of a 3D emission scan that lasted 8 hours. A 2D transmission scan, a 3D blank scan, and a 3D normalization scan on the standard Germanium cylinder provided by CTI PET systems were also acquired. Two sets of scans were acquired, one with scatter correction turned on and one with scatter correction turned off.

Results

Direct and oblique planes 11 were selected at random to compare the effects of scatter correction. As can be seen in Figures 9,10, the Klein-Nishina scatter algorithm accurately accounts for the scatter tails of the data without the assumption of spatial

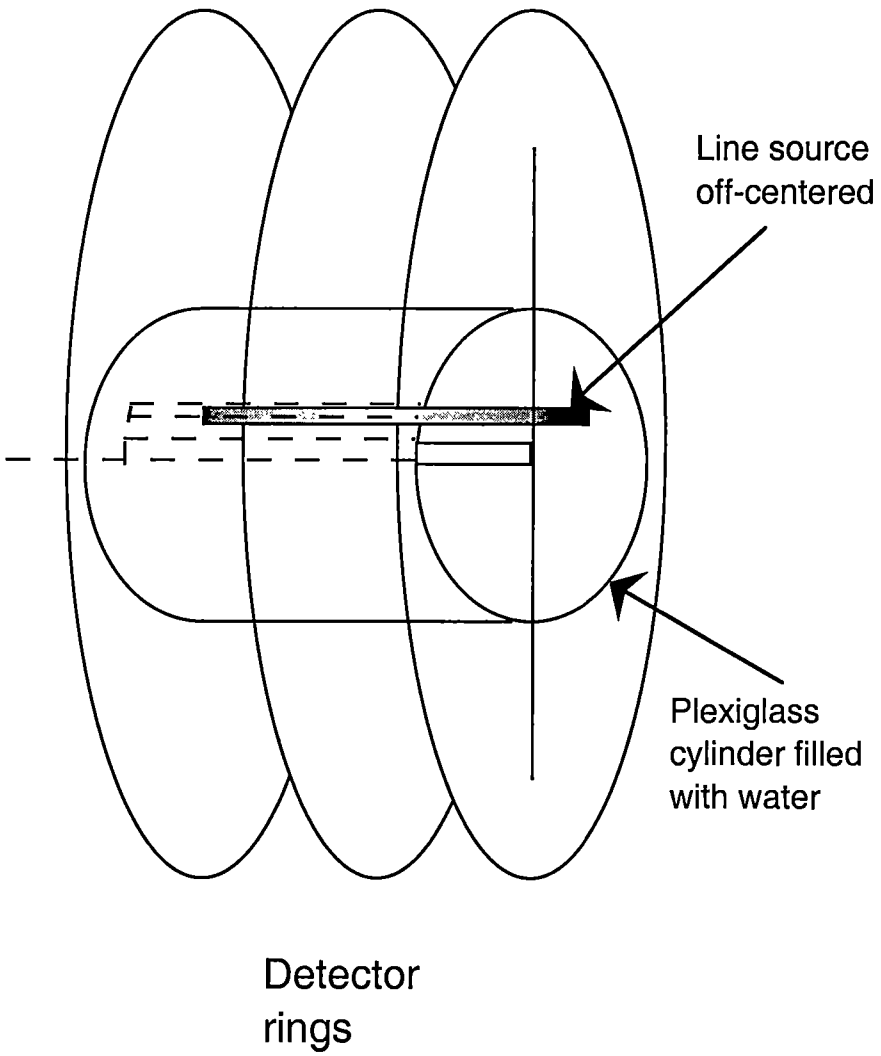


Figure 8 : This figure shows the experimental setup for studying the Klein-Nishina based scatter correction model.

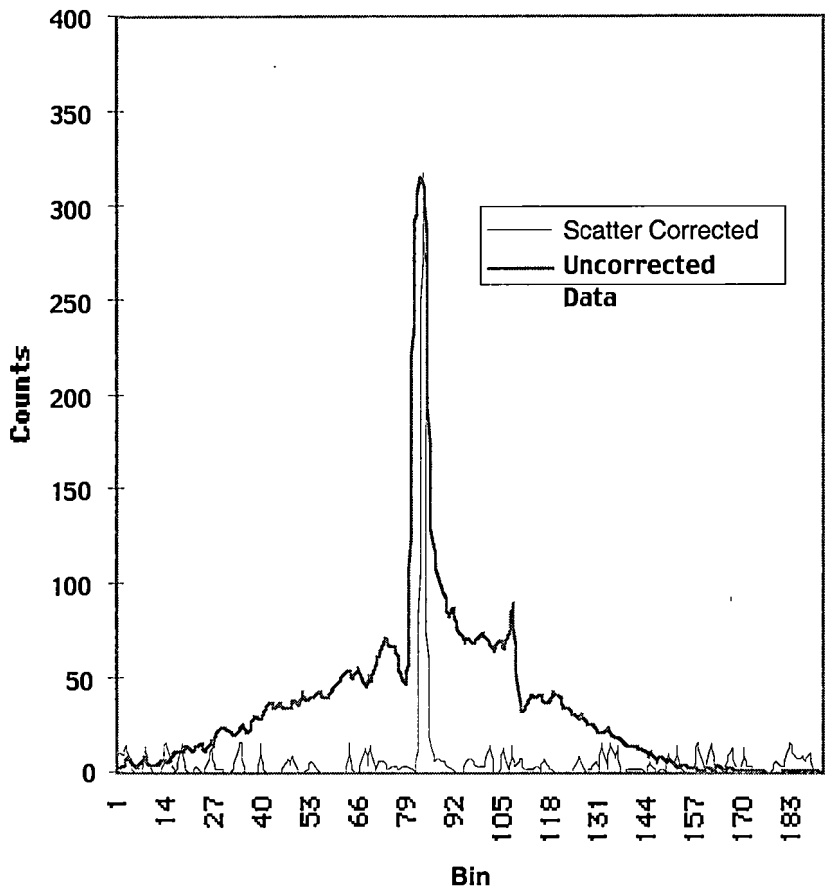


Figure 9 : The center profiles of sinograms of plane 11 in segment-0. The scatter correction has been performed by CTI's implementation of the Klein-Nishina method of scatter-correction. The scatter correction is quite accurate despite the fact that the line source was off-center in the scanner.

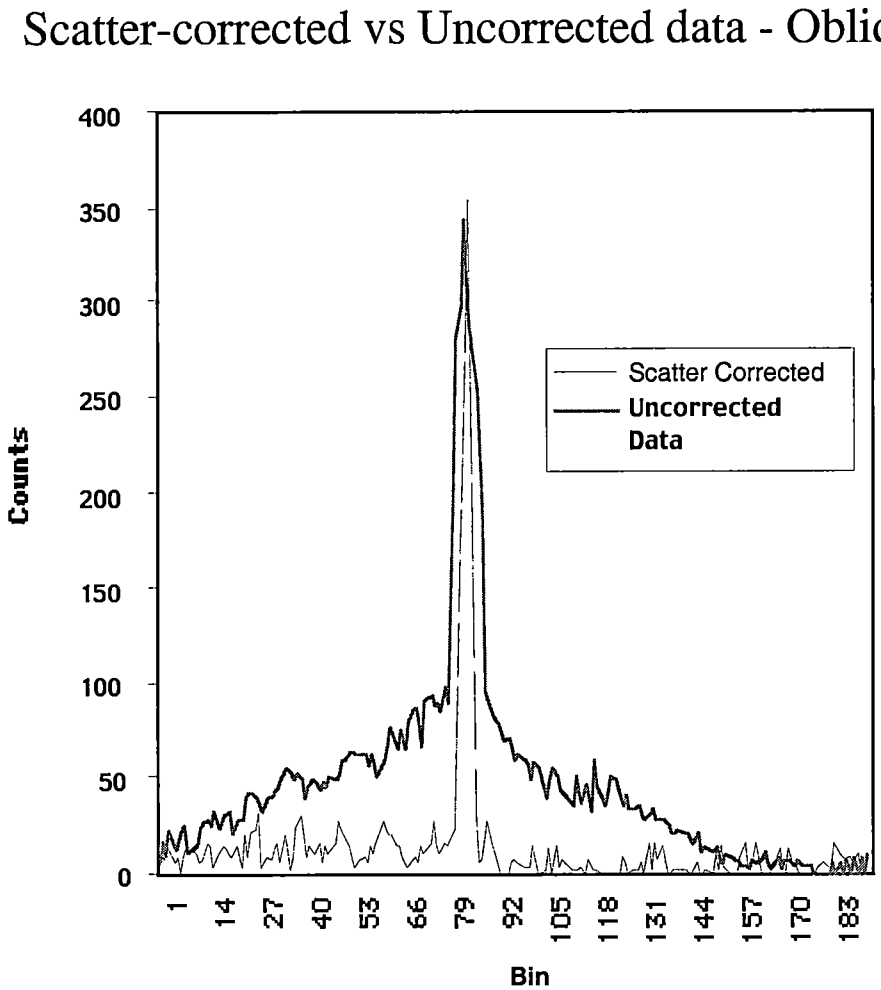


Figure 10 : The center profiles of oblique sinograms of plane 11 in segment-1. See Figure 9 for details.

invariance. Efforts are currently underway to modify Ollinger's Scatter correction code to work for the 921 scanner on which the data was acquired at the University of Tennessee Medical Center.

CHAPTER 3

Image Reconstruction

Image data is collected in the form of projections. Each projection is a collection of data bins, each of which is a line integral sum along a straight path through the object being imaged (Figure 11). In PET, the emissive properties of injected radio-nuclei in the patient's body are used to obtain the projection data. Upon detection, a measurement representing the line integral of the absorption distribution along each path is obtained. This collection of line integrals for each angle between 0 and π radians is known as a sinogram. The next section describes the theory behind the reconstruction of images from sinograms.

Direct Fourier Methods

Direct Fourier methods can be used to reconstruct the image from the projection data. To describe the implementation of the reconstruction, some results must first be stated and explained.

Based on the nature of data collection as described, the projection coordinate system (s,θ) is important to the analysis of the data. We also briefly present the Radon transform to understand how to convert between the (s,θ) system and the Cartesian coordinate (x,y) system.

Radon Transform (Jain 1989)

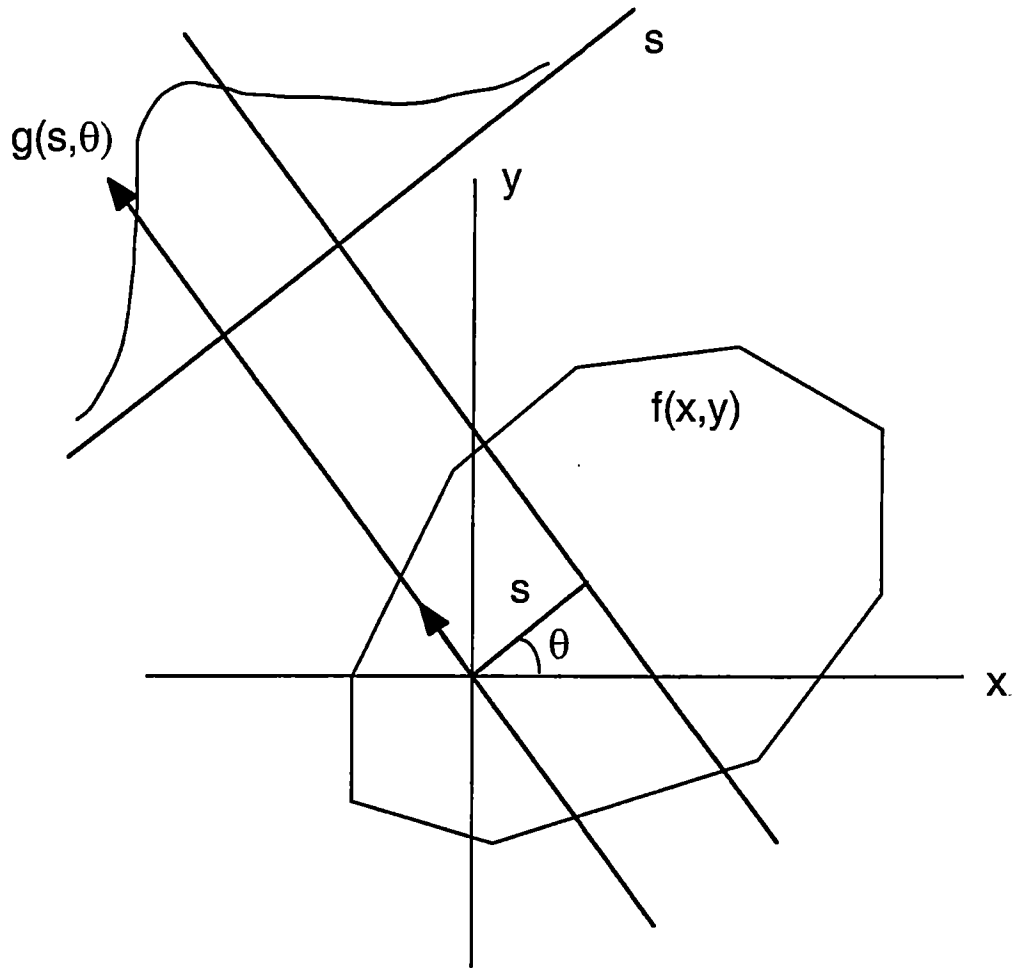


Figure 11 : Projection imaging geometry

The Radon transform of a function f(x,y) is defined as its line integral along a line inclined at an angle θ from the y-axis and at a distance s from the origin.

$$g(s,\theta) = \iint f(x,y)\delta(x\mathrm{Cos}\theta + y\mathrm{Sin}\theta - s)dxdy$$

$$g(s,\theta) = \int f(s\mathrm{Cos}\theta - u\mathrm{Sin}\theta, s\mathrm{Sin}\theta + u\mathrm{Cos}\theta)du$$

$$-\infty < s < \infty$$

$$0 \le \theta < \pi$$

The Radon transform maps the spatial domain (x,y) to the projection domain (s,θ).

Back-Projection Operator

Associated with the Radon Transform is the backprojection operator, defined as:

$$b(x,y) = Bg = \int_0^{\pi} g(x\mathrm{Cos}\theta + y\mathrm{Sin}\theta, \theta)d\theta$$

Backprojection represents the accumulation of the ray-sums of all the rays that pass through the image point (x,y). The backprojection operator maps a function of (s,θ) coordinates into a function of spatial (x,y) coordinates. It can be shown that the back-projected Radon transform is an image of f(x,y) blurred by the point spread function $1/(x^2+y^2)^{1/2}$.

Projection Theorem

The 2D Fourier transform of a function and the 1-D Fourier transform of its Radon transform are related. The 1D-FT with respect to s of the projection $g(s,\theta)$ is equal to the central slice, at angle θ, of the 2D-FT of the object $f(x,y)$.

$$FT[g(s,\theta)] = FT[f(x,y)]$$
$$S_\theta(\omega) = F(\omega,\theta)$$

Filtered Backprojection

The image $f(x,y)$ can be represented in terms of its 2D Fourier Transform as:

$$f(x,y) = \int_0^{\pi}\int_{-\infty}^{\infty} |\omega| F(\omega Cos\theta, \omega Sin\theta) e^{j2\pi(xCos\theta + ySin\theta)} d\omega d\theta$$

Using the Projection Theorem, $f(x,y)$ can be written as :

$$\hat{P}_\theta(s) = \int_{-\infty}^{\infty} |\omega| S_\theta(\omega) e^{j2\pi\omega s} d\omega$$

$$f(x,y) = \int_0^{\pi} \hat{P}_\theta(s) d\theta$$

This is the filtered backprojection of the projection data integrated over all angles θ. So, the image $f(x,y)$ is obtained from the projection data $P(s,\theta)$ by taking its 1D-FT and filtering it with the ramp filter $|\omega|$ and inverse Fourier transforming the result (Figure 12) which is finally backprojected over all θ to give $f(x,y)$ (Figure 13). In practice other ramp filters

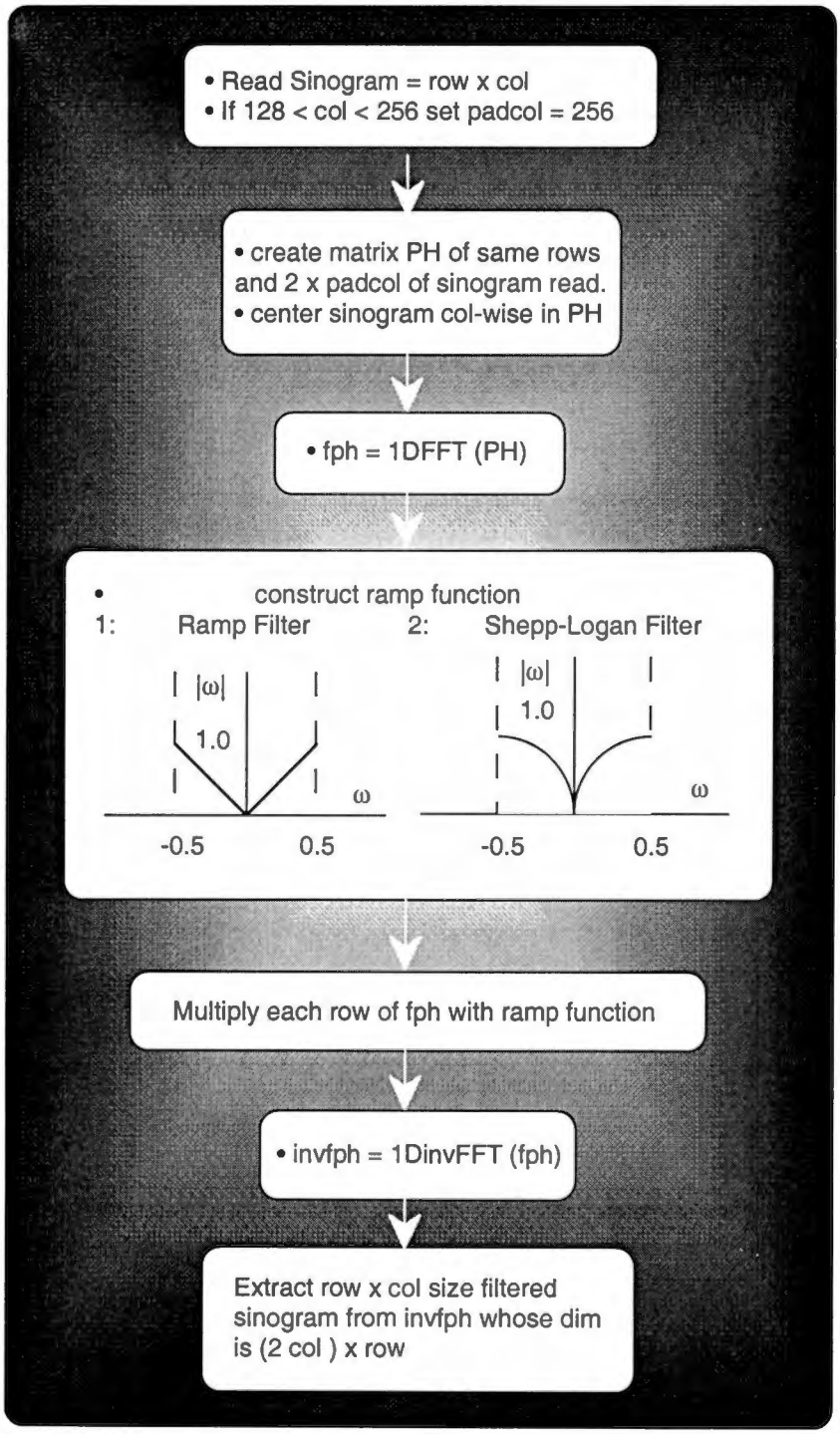


Figure 12 : Flowchart for filtering sinogram before 2D backprojection

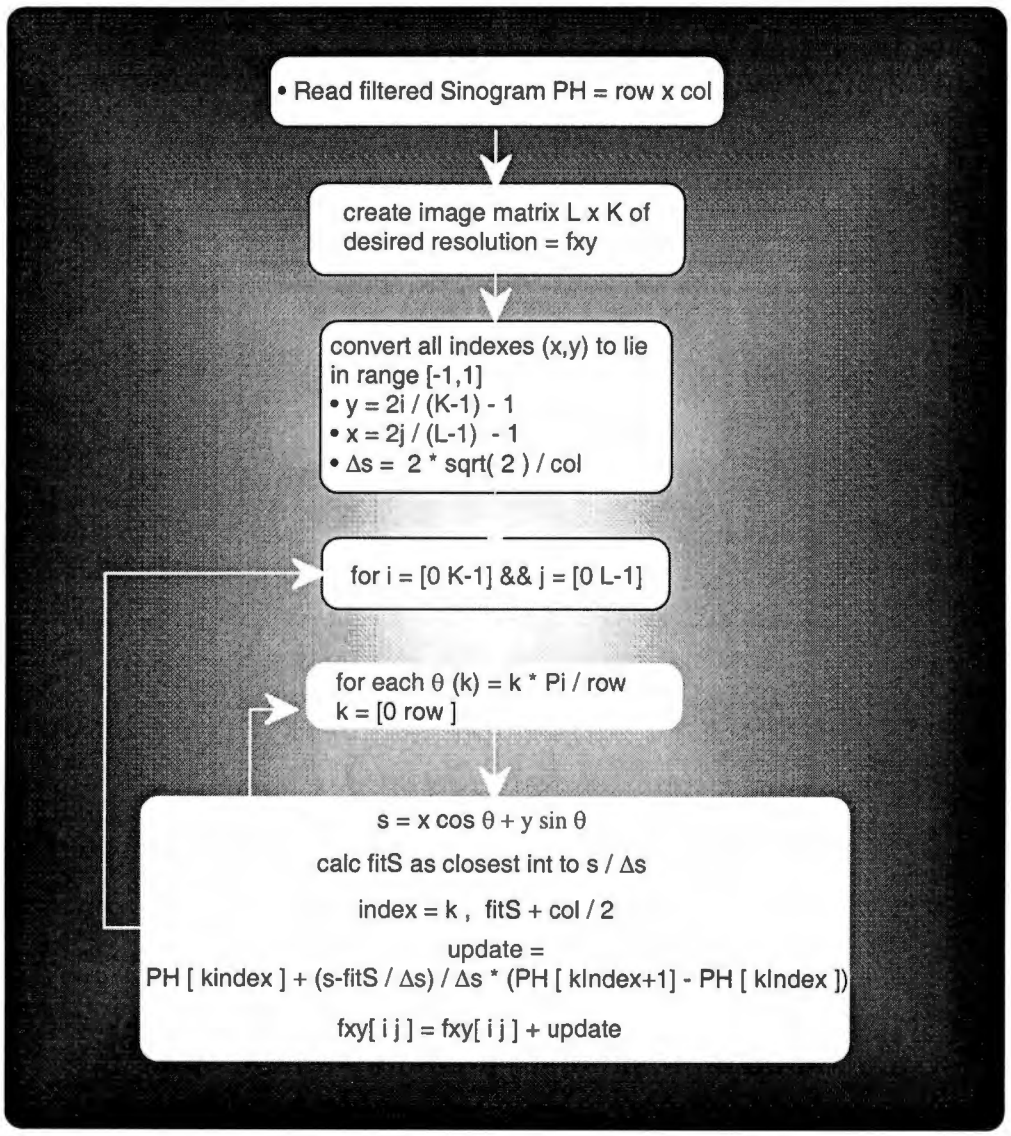


Figure 13 : Flowchart detailing backprojection of filtered sinogram into image.

than $|\omega|$ with gentler roll-off character such as the Shepp-Logan filter, are used.

Three- Dimensional Image Reconstruction

So far all data acquired has been in a 2D mode. This means that septa were extended between detector rings during PET data acquisition so that data from the source was acquired only in direct planes. Ring X's detector elements recorded only those coincidence events that occurred in the plane described by all diameters of Ring X, which are the Lines of Response (LOR) (Figure 14).

Another method of data acquisition is in the 3D mode when inter-ring septa are withdrawn and all detector rings record coincidence events from any plane within the ring volume (Figure 15). The advantage of 3D acquisition is that much more data is acquired in the same amount of time leading to potentially better signal-to-noise ratio (SNR).

CTI PET 3D Data Format (Defrise,1997; Swain 1998) (Figure 16)

CTI PET scanners acquire 3D data with septa withdrawn for coincidences between all N rings. The 921 model at UT Medical Center has 24 rings. So, one sinogram is acquired for each pair of 24 rings (I , J). This data can be organized as shown in Figure 16, with each (I , J) cell representing the oblique sinogram corresponding to coincidences between the ith and jth detector rings. However to save space and processing time, sinograms adjacent to each other as specified by a pre-defined span are

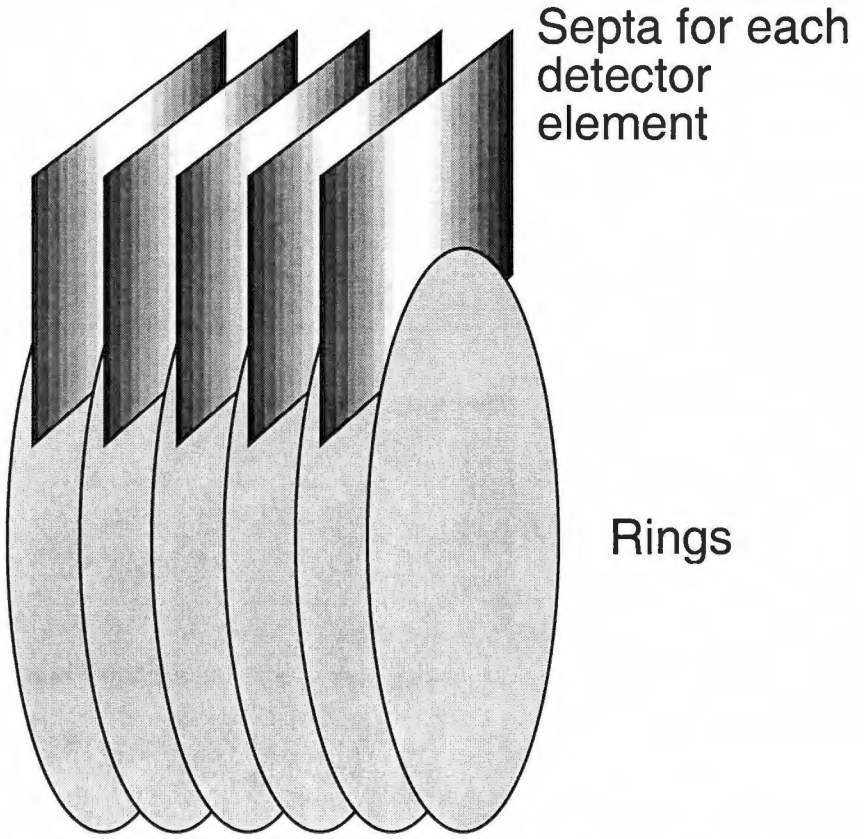


Figure 14 : Two Dimensional PET data acquisition. All coincidence data is acquired in direct planes corresponding to planes of rings separated by lowered septa between each pair of detector elements of neighboring rings.

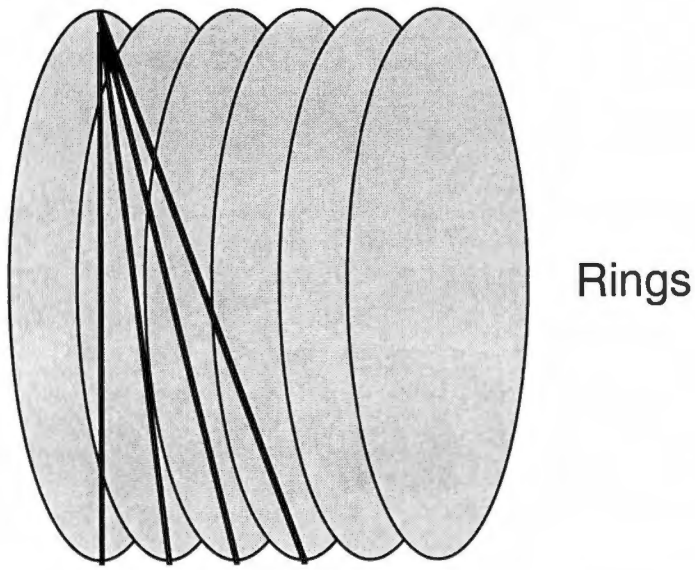


Figure 15: Three Dimensional PET data acquisition. All coincidence data is acquired in all possible planes contained within imaging volume of all rings corresponding to N(N-1) oblique planes for N rings. This data is then reduced to segments 0,1,2.

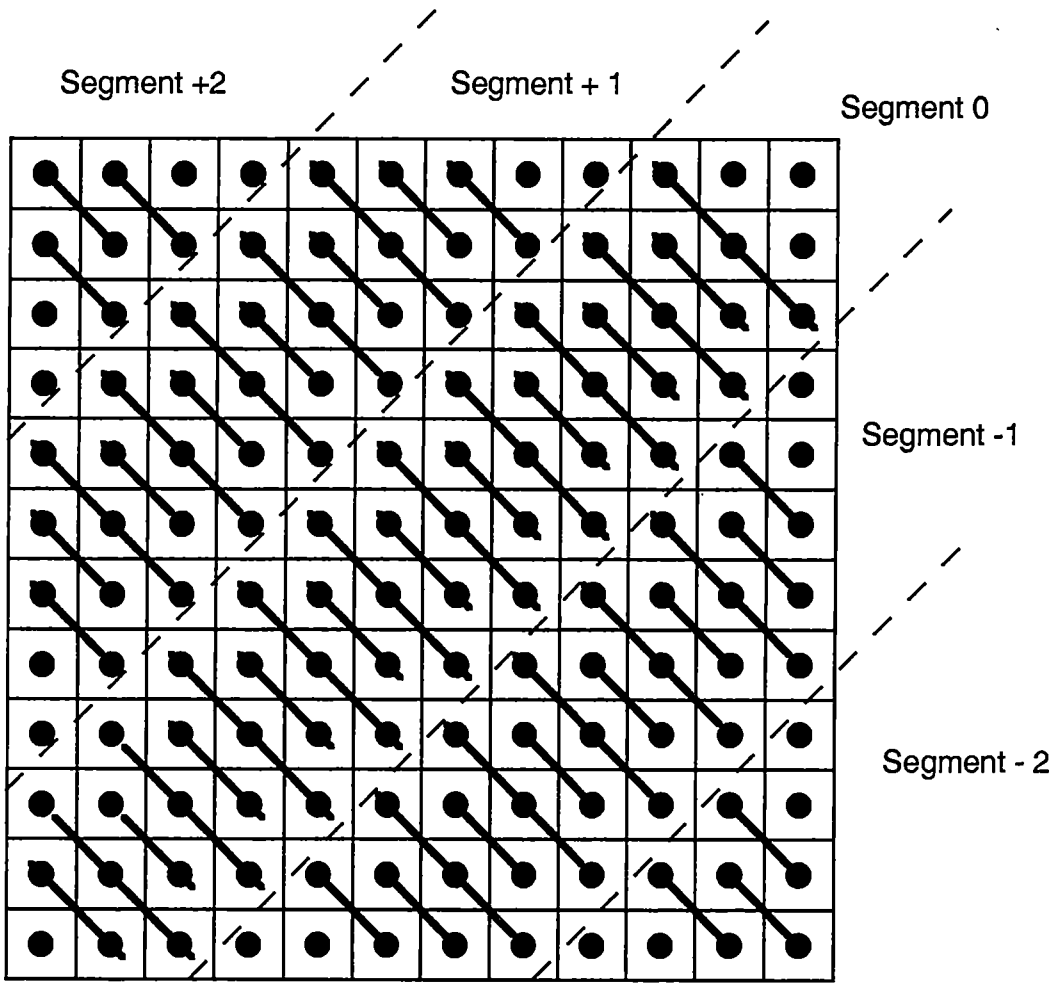


Figure 16 : Schematic representation of 3D data acquired by 12-ring scanner. The vertical and horizontal axis correspond, respectively, to the integers j and i of two rings in coincidence. Each square corresponds to one oblique sinogram (i,j). Sets of oblique sinograms linked by solid line segments are added together to form aggregate sinograms. (Adapted from (Defrise, 1997)).

added to each other to create aggregate sinograms. In figure 16, all sinograms connected by solid lines are added to each other to form a new sinogram. Each pair of adjacent dotted lines enclose sinograms of fixed ring separation. For example, all aggregate sinograms enclosed within the two dotted lines along the diagonal correspond to direct sinograms of ring separation 0. This is known as the set of sinograms of segment 0. The sinograms in each segment are stored in increasing ring number order. Aggregate sinograms immediately neighboring segment 0 are of ring difference ±1 and correspond to segment 1. Similarly all sinograms outside the limits of segment 1 separated by the dashed boundaries correspond to segment 2 and correspond to ring difference ± 2. The 921 scanner only stores data corresponding to segment 0, ±1, and ±2 in that order preceded by a 2 Kilobyte header for a 3D data set.

3D Image Reconstruction (Defrise, 1997)

There are three main types of 3D image reconstruction algorithms: analytical, rebinning, and statistical algorithms. Among analytical algorithms, the most popular seems to be the 3D Reprojection algorithm (3DRP) which is a simple extension of the 2D filtered backprojection algorithm. The 3DRP algorithm (Kinahan, 1989) first reconstructs the image volume roughly from the available direct plane or segment-0 data set. It then reprojects out the reconstructed image volume into those outlying spaces from which data has not been acquired due to ring-volume limitations. This "extra" projection data is used

to augment the existing 3D sinogram data set and then in accordance with the filtered backprojection technique all data is processed to create the image space. Rebinning techniques can be both approximate and exact. A rebinning algorithm is defined as an algorithm which sorts (rebins) the 3D data into a stack of ordinary 2D data sets of sinograms. This converted 2D data set can then be reconstructed using any 2D reconstruction algorithm (Figure 17). Statistical techniques such as EM (Shepp, 1982) and EM-MAP (Mumcuoglu, 1996) iteratively maximize likelihood functions and are computationally expensive. We use the FORE rebinning algorithm which is an approximation of an exact rebinning technique to remap 3D data into 2D data sets.

Exact rebinning method for 3D image reconstruction

Consider a cylindrical scanner of radius R and length L whose z-axis is defined as the axial direction (Figure 18). Any plane orthogonal to the z-axis is a transaxial plane. The distribution of the radioactive tracer is f(x,y,z) defined in a cylindrical field-of-view Ω with a radius $R_\Omega < R$ and with same axis and length as the scanner. The integral of f(x,y,z) is measured along LOR's joining any two detectors, and the reconstruction problem lies in estimating f(x,y,z) from this data. The data acquired in 3D mode by the scanner is parametrized as $P(s,\phi,z,\delta)$, where s corresponds to the orthogonal distance from the center of the scanner to the LOR, ϕ is the transaxial angle of the LOR, z is

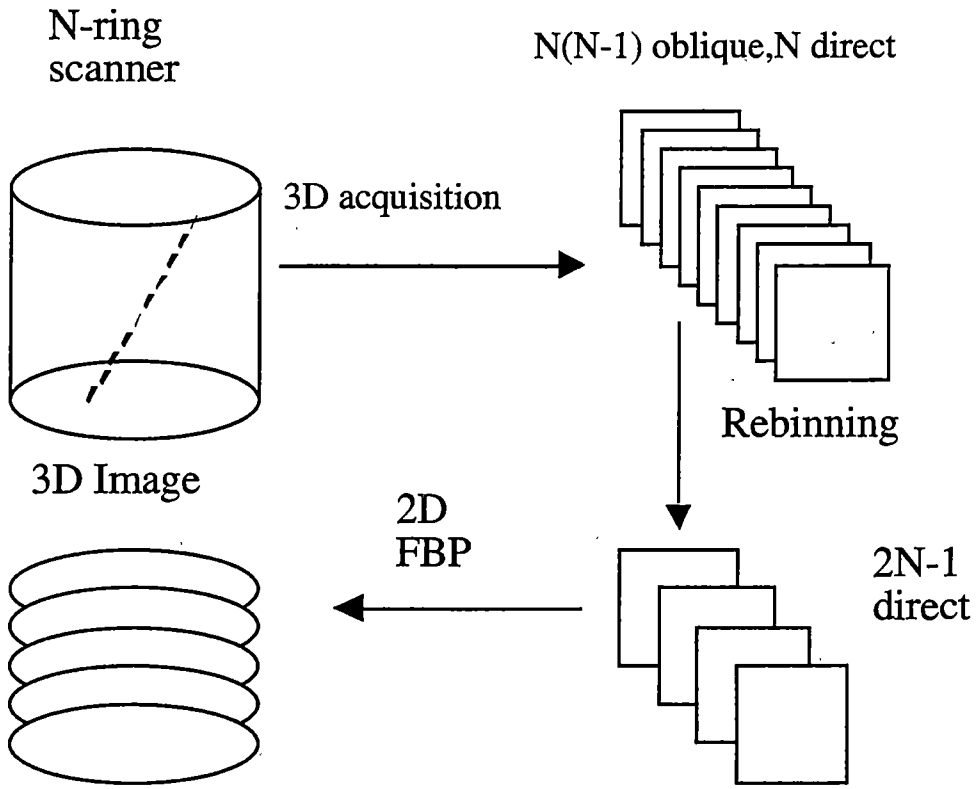


Figure 17 : Principle of rebinning algorithms

the point at which the LOR intersects the z-axis and δ is proportional to the separation on the z-axis of the two rings in coincidence for the LOR (Figure 18).

Then it can be shown (Defrise, 1997) that the relation between the 2D Fourier transforms of the oblique and direct planes is:

$$P_{ft}(\omega,k,\omega_z,\delta) = \exp\{-ik \arctan(\frac{\delta\omega_z}{\omega})\} \cdot P_{ft}(\omega\sqrt{1+\frac{\delta^2\omega_z{}^2}{\omega^2}},k,\omega_z,0)$$

This allows the rebinning of every oblique plane into a corresponding direct plane in Fourier space. Taking the inverse transform of all subsequent direct planes yields a rebinned 2D sinogram data set which can be reconstructed using any 2D technique.

Approximate Rebinning Algorithms (Defrise, 1997)

The above exact rebinning formula can be rewritten as:

$$P_{ft}(\omega,k,\omega_z,\delta) = \exp\{-i\Delta\phi\} \cdot P_{ft}(\omega\chi,k,\omega_z,0)$$
$$\Delta\phi = \text{phase shift} = k \cdot \arctan\ \alpha$$
$$\chi = \text{frequency scaling} = \sqrt{1+\alpha^2}$$
$$\alpha = \frac{\delta\omega_z}{\omega}$$

A class of rebinning algorithms of increasing accuracy can be obtained by considering truncated Taylor expansions in α.

First Order approximation in α: FORE algorithm (Defrise, 1997)

Keeping terms linear in α and noting that:

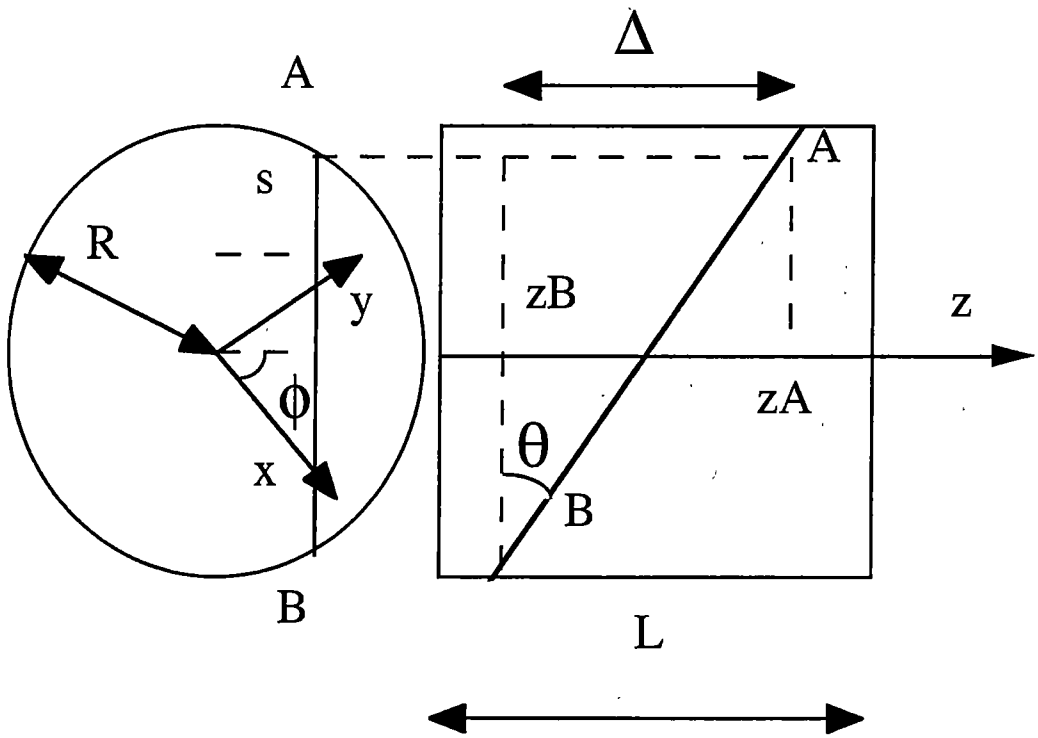


Figure 18 : Geometry of a cylindrical PET scanner. Transaxial view (left) with the standard sinogram variables s and ϕ parameterizing the straight line AB. Longitudinal section (right) with the axial variables z and Δ.

$$\Delta\phi = k\alpha + O(\alpha^3)$$
$$\chi = 1 + O(\alpha^2)$$

we get:

$$P_{ft}(\omega,k,\omega_z,\delta) \approx \exp\{-ik\frac{\delta\omega_z}{\omega})\} \cdot P_{ft}(\omega,k,\omega_z,0) + O(\alpha^2)$$

As the only dependency on the axial frequency ω_z is a linear phase shift, we get:

$$P_{ft}(\omega,k,z,\delta) \approx P_{ft}(\omega,k,z-\frac{k\delta}{\omega},0)$$

This is the Fourier Rebinning approximation. It relates the 2D Fourier transform of an oblique sinogram (z,δ) to the 2D Fourier transform of the direct sinogram of a slice shifted axially by a frequency dependent offset $\Delta z = -k\delta / \omega$.

Geometrical interpretation of the Fourier rebinning equation (Defrise, 1997)

The original derivation of Fourier rebinning was based on the frequency-distance relation, a property of the 2D Radon transform discovered by Edholm (Edholm, 1986). Consider the 2D Fourier transform $P(\omega,k,z,\delta)$. The frequency-distance relation states that the value of P at the frequency (ω,k) receives contributions mainly from sources located at a fixed distance $t = -k / \omega$ along the lines of integration. Parameter "t" represents the signed distance measured on a transaxial projection of the LOR, from its midpoint

(Figure 19A). If the activity is contained within a FOV radius R_Ω, then the distance t of any source along any LOR cannot exceed R_Ω, Hence, the Fourier transformed data must vanish for $|t| = |k / \omega| > R_\Omega$ (Region 2, Figure 19B). If "t" lies within the FOV, the source contribution can be rebinned to the two nearest direct plane neighbors to z' (Region 1, Figure 19B). If "t" lies within the FOV of the object imaged, but w and k are so small that k/w cannot be significantly determined, then the oblique plane contributes only to the direct plane which intersects the z-axis as itself (Region 3, Figure 19B).

FORE Algorithm (Defrise, 1997)(Figures 20,21)

The FORE algorithm is described by the flowchart in Figures 20,21. The general steps are as follows:

1: Read in all direct and oblique sinograms. Zero pad in the s-direction and interpolate in the ϕ direction to get powers of 2 number of elements in each direction for each sinogram.

2: Calculate the 2D FFT of each sinogram – P_{FT} , initialize Prebin which will contain the 2D rebinned sinograms, and Pnorm which is used to normalize Prebin.

3: For each sinogram (z, δ) (Region 2 – High frequency, $|k / \omega| > R_\Omega$) has no contribution by previous section's explanation):

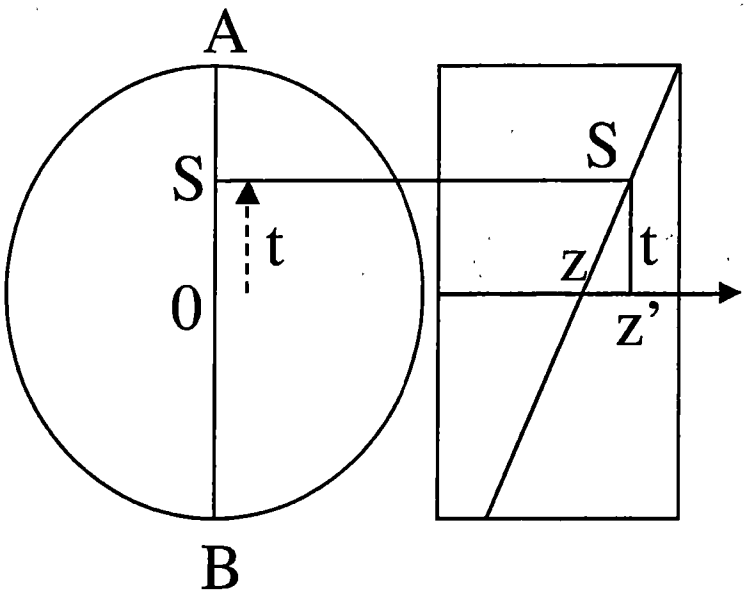


Figure 19A: Geometric interpretation of Fourier rebinning with the help of the Fourier-distance relation.

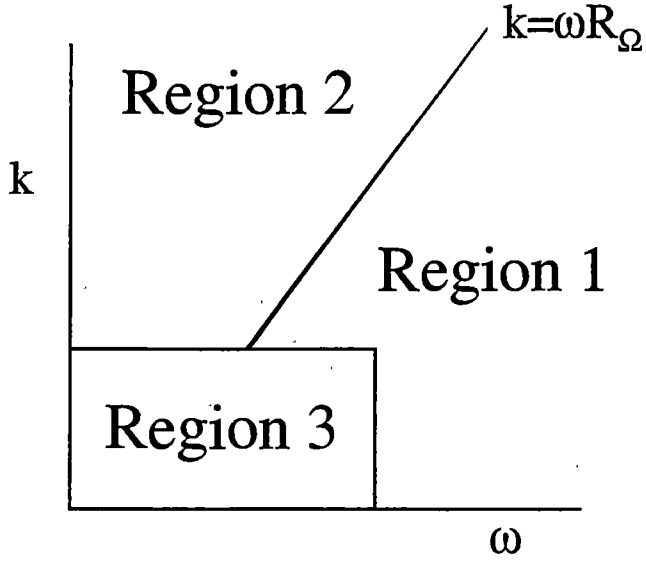


Figure 19B: Depending on ω,k sources will contribute in one of 3 ways to the oblique sinogram in Figure 19A. So there will be one of 3 types of rebinning.

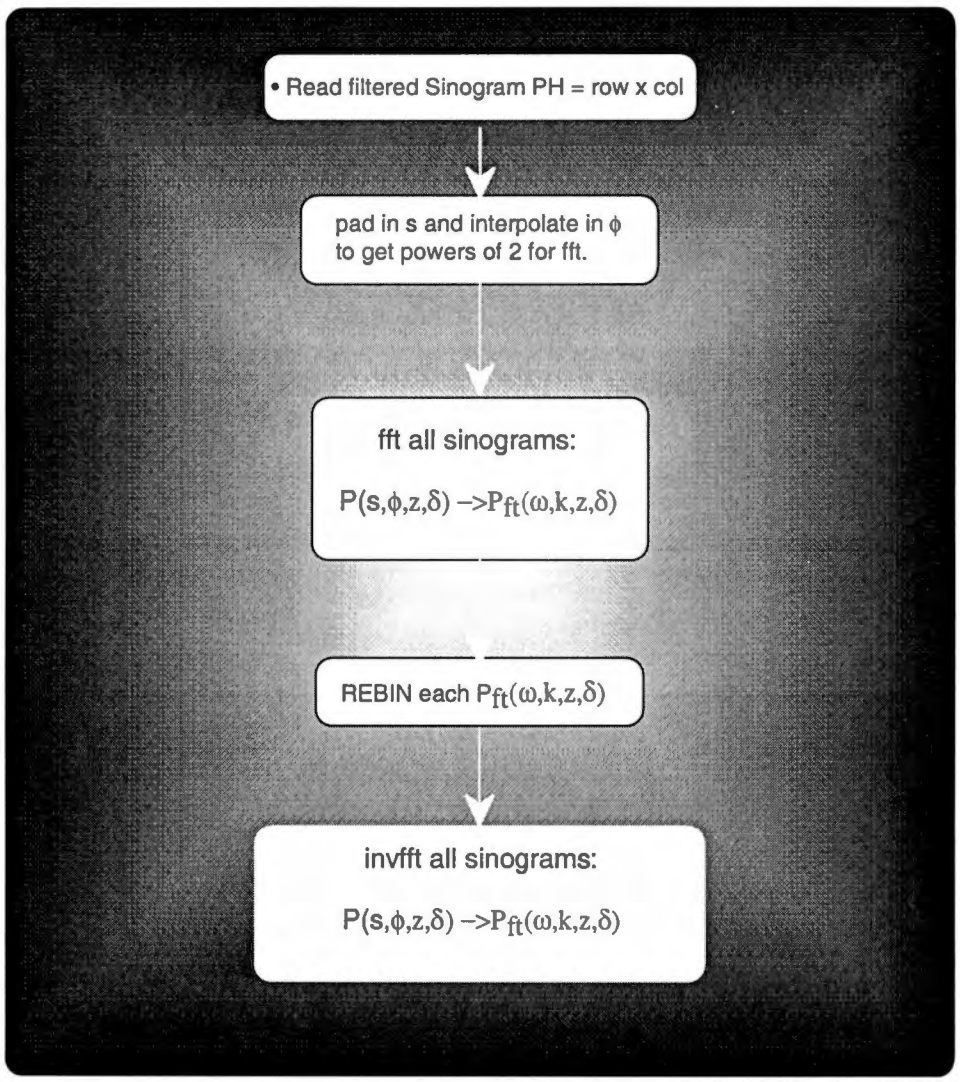


Figure 20: General FORE algorithm flowchart

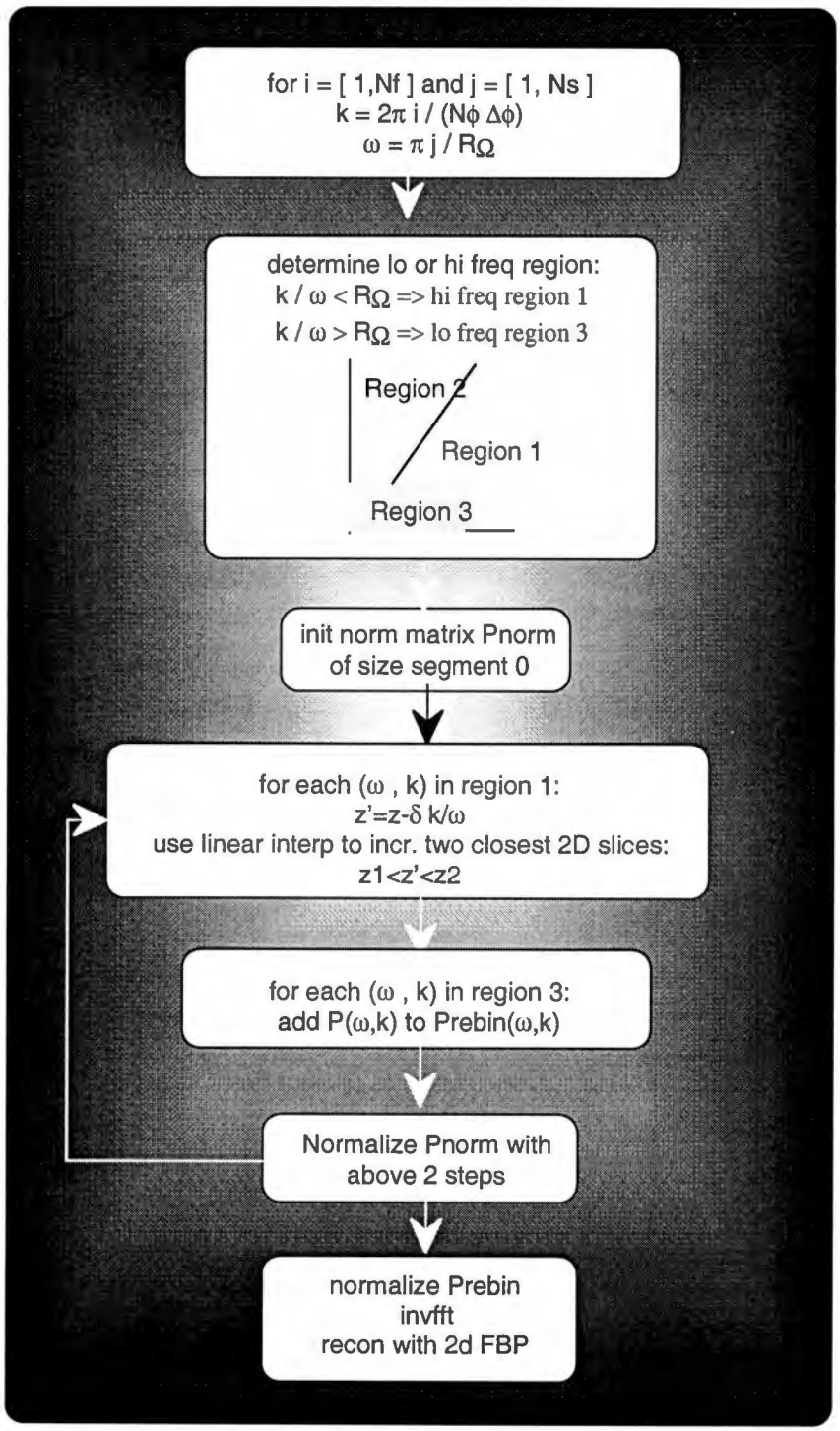


Figure 21 : Rebinning algorithm flowchart

A: For each sample (ω,k) in region I: (High frequency $|k / \omega| < R_\Omega$)

$z' = z - \delta k / \omega$ for $z1 < z' <= z2$

Add $((z2 - z') * P_{FT})$ to $Prebin(\omega,k,z1)$

Add $((z'-z1) * P_{FT})$ to $Prebin(\omega,k,z2)$

B: For each sample (ω,k) in region 3: (FORE does not apply,

$k<k_{LIM}, \omega< \omega_{LIM}$), Add P_{FT} to $Prebin(\omega,k,z)$

4: Normalize Prebin with Pnorm which has been incremented similar to Prebin in step 3A or 3B. Pnorm was initially all initialized to 1.0.

5: Take the inverse 2D FFT of Prebin to get stack of rebinned sinograms.

6: Reconstruct each slice with a 2D reconstruction algorithm, e.g. FBP.

Experiment:

A PET scan was done on a line source of FDG radioactive source with a half life of 117 minutes. The line source was a syringe about 6 mm in diameter and 20 cm in length. The scatter medium was clinically pure de-ionized water at room temperature in a Plexiglas cylinder as shown in Figure 8. Gamma rays emitted due to positron annihilation in the line source and the surrounding water are emitted in pairs 180° to each

other to opposing detector elements. The detector electronics measure coincidences within an energy threshold and save the data as sinograms.

The scan series consists of a 3D and a 2D emission scan of length 10 minutes. The 3D data set was reconstructed with the FORE algorithm and compared to a 2D FBP reconstruction of the 2D data set. As can be seen, the FORE reconstruction image is cleaner with more SNR than the 2D FBP reconstruction (Figure 22).

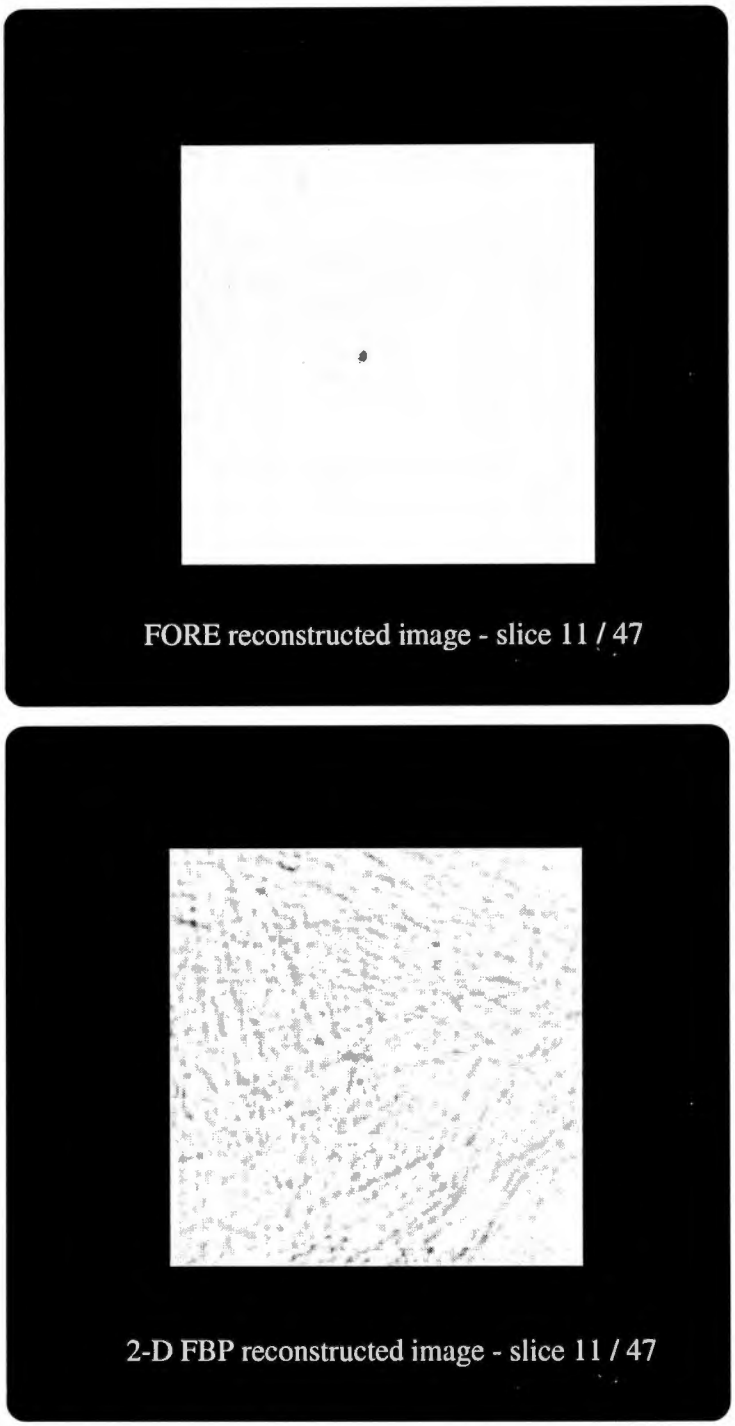


Figure 22 : FORE versus 2D FBP reconstruction. Both were 10 minute scans – The FORE scan was acquired without septa and the FBP scan was acquired with septa.

CHAPTER 4

Image Registration

Image registration is the process by which one image, designated as the reference image, is used as a guide to align another image known as the target, such that common key landmarks in the two images coincide with respect to the common frame of reference of the reference image. This is useful in radiology where different data modalities such as MRI and PET yield complementary information. But, since the scans have been taken under different conditions and at different times it is usually the case that such images cannot be simply merged. Image registration is the technique by which one image is translated iteratively with the calculation of a cost function in order to achieve as good a match as possible. The package used to do this is called AIR (Automated Image Registration) (Woods, 1992; Woods, 1993; Woods, 1998A; Woods, 1998B)

Automated Image Registration

The Automated Image Registration (AIR) package is primarily designed to solve several different registration problems that arise in tomographic data sets:

- Intrasubject, intramodality registration (e.g., PET to PET or MRI to MRI)
- Intrasubject, intermodality registration (e.g., PET to MRI)
- Intersubject registration (e.g. subject to subject or subject to atlas template)

Intrasubject registration of brain images uses a rigid-body model. Intermodality registration has been validated for some (MRI-PET), but not all modalities. Intersubject registration can be performed using any of a variety of linear or nonlinear models to register different subjects to one another. These models may also be useful for intrasubject registration of organs that are more deformable than brain or for tracking intrasubject developmental changes over time.

Once the registration parameters are known, the AIR package allows the data to be resampled to generate a final image using any of the following interpolation models: nearest neighbor, trilinear, windowed sinc, mixed linear/windowed sinc, unwindowed sinc, chirp-z, mixed linear/chirp-z.

The AIR package includes automated routines for aligning and reslicing tomographic image data. In addition, a number of utility routines and error checking routines are provided. The routines are invoked as standard UNIX commands. In addition, a series of C subroutines which comprise the AIR library are provided. The AIR library can be used to easily incorporate automated image registration into site specific programs adapted to particular needs. AIR 3.0 also includes graphical user interfaces for two of the most frequently used programs. These interfaces are written in Tcl/Tk.

Synopsis of the programs

The AIR 3.0 package includes two programs for automated registration of images. The first of these, **alignlinear**, includes 2D and 3D variants of all linear spatial transformation models, including rigid-body models, global rescaling models, and affine models. It generates a file, referred to here as a ".air file", that contains linear transformation parameters for resampling one of the images to match the other. The second alignment program, **alignwarp**, includes 2D and 3D variants of second, third, fourth, and fifth order nonlinear polynomial spatial transformation models. It generates a file, referred to here as a ".warp file", that contains nonlinear transformation parameters for resampling one of the images to match the other.

The program **reslice** will use the registration parameters in a .air file to resample the reslice file (which is explicitly identified in the .air file) to match the standard file. Nearest neighbor, trilinear, or various forms of sinc interpolation can be used. The program **reslice_warp** provides similar functionality for .warp files.

The alignment programs depend upon the image headers for certain information about file dimensions and sizes. The program **makeaheader** creates header files for AIR. The program **scanheader** will display the relevant information contained within an image header so that it can be verified that the information is correct.

For use with AIR, individual slices from an image must be concatenated into a single image volume. The programs **reunite** and **separate** facilitate conversion between data formats that store each slice in a separate file and the multiimage format required by AIR. The programs **scanair** and **scan_warp** allow the display of information contained in .air and .warp files.

Because the .air and .warp files are stored separately from the image files, an additional level of file identification has been incorporated into these files. In addition to the names of the files, a ten digit identifier is computed based on the data in the file. This identifier is displayed along with the other information shown by **scanair**. In the event that one is unsure that a file is the file used to derive a set of registration parameters, one can use the program **identify** to compute the ten digit number that corresponds to a given data file.

Description of the .air file

The **.air** file computed by the **align** code from the reference image contains the matrix which when applied to the target image, transforms it into an image whose coordinate system approximately matches that of the reference image. A regular 3D coordinate system is not used in computing the **.air** file. Instead a **homogenous** coordinate system is used.

Homogenous Coordinates

Homogenous coordinates utilize a mathematical trick to embed three-dimensional coordinates and transformations into a four-dimensional matrix format. As a result, inversions or combinations of linear transformations are simplified to inversion or multiplication of the corresponding matrices. Homogenous coordinates also make it possible to define perspective transformations. Instead of representing each point (x,y,z) in three-dimensional space with a single three-dimensional vector:

$$\begin{bmatrix} x \\ y \\ z \end{bmatrix}$$

homogenous coordinates allow each point (x,y,z) to be represented by any of an infinite number of four dimensional vectors:

$$\begin{bmatrix} T*x \\ T*y \\ T*z \\ T \end{bmatrix}$$

The three-dimensional vector corresponding to any four-dimensional vector can be computed by dividing the first three elements by the fourth, and a four-dimensional vector corresponding to any three-dimensional vector can be created by simply adding a fourth element and setting it equal to one.

Homogenous coordinate transformation matrices operate on four-dimensional homogenous coordinate vector representations of traditional three-dimensional

coordinate locations. Any three-dimensional linear transformation (rotation, translation, skew, perspective distortion) can be represented by a 4x4 homogenous coordinate transformation matrix. In fact, because of the redundant representation of three space in a homogenous coordinate system, an infinite number of different 4x4 homogenous coordinate transformation matrices are available to perform any given linear transformation. This redundancy can be eliminated to provide a unique representation by dividing all elements of a 4x4 homogenous transformation matrix by the last element (which will become equal to one). This means that a 4x4 homogenous transformation matrix can incorporate as many as 15 independent parameters.

The generic format representation of a homogenous transformation equation for mapping the three dimensional coordinate (x,y,z) to the three-dimensional coordinate (x',y',z') is:

$$\begin{bmatrix} T'\cdot x' \\ T'\cdot y' \\ T'\cdot z' \\ T' \end{bmatrix} = \begin{bmatrix} T''\cdot a & T''\cdot b & T''\cdot c & T''\cdot d \\ T''\cdot e & T''\cdot f & T''\cdot g & T''\cdot h \\ T''\cdot i & T''\cdot j & T''\cdot k & T''\cdot m \\ T''\cdot n & T''\cdot p & T''\cdot q & T'' \end{bmatrix} * \begin{bmatrix} T\cdot x \\ T\cdot y \\ T\cdot z \\ T \end{bmatrix}$$

If any two matrices or vectors of this equation are known, the third matrix (or vector) can be computed and then the redundant T element in the solution can be eliminated by dividing all elements of the matrix by the last element. Various transformation models can be used to constrain the form of the matrix to transformations with fewer degrees of

freedom. For example, translations can be represented by the 4x4 homogenous coordinate transformation matrix:

$$\begin{bmatrix} 1 & 0 & 0 & \text{x-shift} \\ 0 & 1 & 0 & \text{y-shift} \\ 0 & 0 & 1 & \text{z-shift} \\ 0 & 0 & 0 & 1 \end{bmatrix}$$

where:

x-shift=translation along the x-axis
y-shift=translation along the y-axis
z-shift=translation along the z-axis

$$\begin{bmatrix} a & b & c & d \\ e & f & g & h \\ i & j & k & m \\ n & p & q & 1 \end{bmatrix}$$ is the matrix that is stored in the .air file.

Spatial Transformation Models

The AIR package uses a variety of spatial models to restrict the type of linear transformation that is being applied when performing registration. Some of the models implemented in AIR 3.0 are:

- 3D linear models: rigid-body (6 parameters), global rescaling (7 parameters), traditional (9 parameters), affine (12 parameters).
- 3D nonlinear models: First order (12 parameters), Second order (30 parameters).
- 2D linear models: rigid-body (3 parameters), global rescaling (4 parameters)
- 2D nonlinear models: First order (6 parameters), Second order (12 parameters)

In the following work presented, 3D linear models were used to perform image registration using the AIR package.

Experimental Results

A GUI system was designed and built using the AMULET toolkit with GNU C++ language. It consists of three interfaces: a file selection GUI, an image parameterization GUI, which allowed images to be coregistered, loaded, and displayed, and their parameters loaded along with details of the coregistration model to be used, and a final GUI which displays the coregistered images with crosshairs to compare matching landmarks (Figure 23,24).

The images used in this run were PET Brain FDG-18 emission and transmission studies with the emission study being used as the reference for coregistration. As is seen (Figure 24) the studies have registered accurately with respect to each other in the final GUI display, proving the success of AIR as a registration solution. The GUI interface provides an effective and convenient method to access AIR's functionality and display the results.

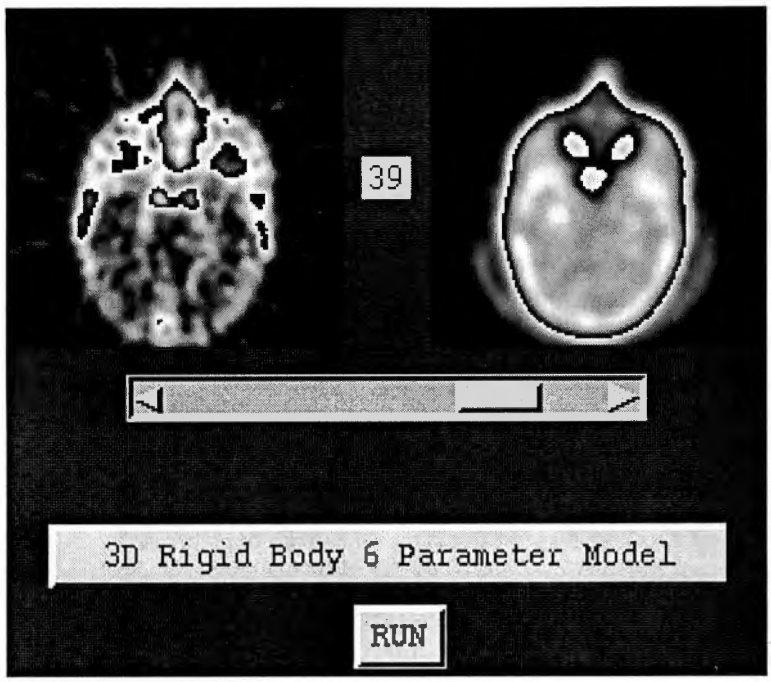


Figure 23 : GUI for setting up AIR coregistration parameters for image sets. The emission study on the left is the reference set.

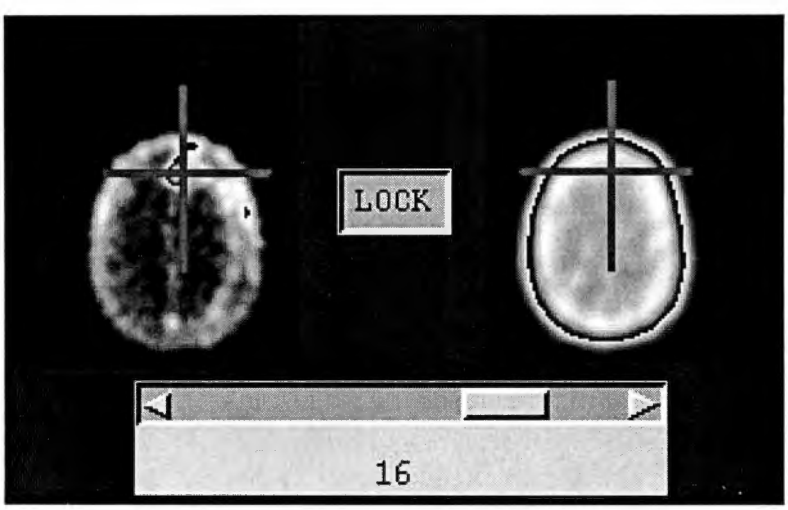


Figure 24 : GUI for displaying reference image set with coregistered transmission study in order to compare relevant features with moveable crosshairs.

CHAPTER 5

CONCLUSION

This study was begun with the intention of designing and developing various software tools to analyze PET images. Several aspects of image acquisition, correction, and analysis were explored.

The graphical interface to all functions was designed as a backbone into which functions could be added or removed as modules, easily and efficiently. Other goals in the design of the interface were to give the user as wide a range of tools as possible to work with and allow him to access these tools easily.

3D PET data offers better SNR compared to 2D data because for a scanner with N rings, N times more data is gathered in 3D mode than 2D. However two problems in particular have prevented the large-scale adoption of 3D PET imaging. One is that of computing power to process huge 3D data sets. Considering the current advances in computational ability, this is not so much of a challenge as it was before. The other major problem is that scatter is a much more serious problem in 3D data acquisition than in 2D. Model based scatter correction techniques have been computationally unfeasible until recently. This is now changing. Studying current scatter correction methods, in particular that of Ollinger's Klein-Nishina based technique was a major goal of this work. As was shown by experiment good results can be obtained by this technique.

2D and 3D image reconstruction techniques were also investigated and an efficient 3D reconstruction technique, the FORE algorithm, was successfully implemented. The standard 2D FBP image reconstruction algorithm was also implemented as a part of the 3D technique. The FORE algorithm was shown to provide good results in reconstructing 3D PET data sets.

Image coregistration is an important technique in medical image analysis because no single imaging modality can provide all required information. The AIR package seems to work well in transforming images from different modalities so as to let them be compared for complementary information. A graphical interface was also designed around the AIR package to allow ease of use.

Several tasks still remain to be implemented. This project was begun with the aim of providing am easily accessible and usable interface to common image processing tasks in a medical environment. One of the means to achieve this goal could be a JAVA based implementation in an internet browser environment. Although the coding would not be difficult, security considerations would demand an extremely robust design. Some tools still need to be added to the interface, such as statistical image reconstruction tools and database access tools. A 3D FBP tool would also be useful as part of a complete image analysis set.

BIBLIOGRAPHY

BIBLIOGRAPHY

Bergstrom M., Eriksson L., Bohm C.,Blomqvist G.,Litton J., (1983). "Correction for scattered radiation in a ring detector positron camera by integral transformation of the projections." Journal of Computer Assisted Tomography **7**: 42-50.

Bond, H. (1998). "Codes for conversion of CTI ECAT format data to raw data." Private Communication, IPL, Radiology, UT Medical Center.

Brad A. Myers, Mcdaniel R., Robert Miller,Alan Ferrency, A. Faulring, Bruce Kyle, Andy Mickish, Alex Klimovitski, P. Doane (1997). "The Amulet Environment: New Models for Effective User Interface Software Development." IEEE Transactions on Software Engineering **23**(6).

Cherry S R, Huang S C (1995). "Effects of scatter on mode parameter estimates in 3D PET studies of the human brain." IEEE Transactions on Nuclear Science **NS-42:** 1174-1179

Defrise Michel, Kinahan P. E., Townsend D W., Sibomana M, Newport D F. (1997). "Exact and Approximate Rebinning Algorithms for 3D PET Data." IEEE Transactions on Medical Imaging **16**(2): 145-158.

Edholm P.R., Lewitt R. M., Lindholm B., (1986). "Novel properties of the Fourier decomposition of the sinogram." Int. Workshop Physics and Engineering of Computerized Multidimensional Imaging and Processing. Proc. SPIE **671**: 8-18.

Evans R D, (1955) "The Atomic Nucleus" (New York: McGraw-Hill)

Grootonk S., Spinks T. J., Jones T.,Michel C.,Bol A. (1991). "Correction for scatter using a dual energy window technique with a tomograph operating without septa." IEEE Medical Imaging Conf. (Santa Fe, 1991): 1569-1573.

Jain, A. K. (1989). Fundamentals of Digital Image Processing, Prentice Hall.

Karp J S, Muehllehner G, Mankoff D A, Ordonez C E, Ollinger J M, Daube-Witherspoon M E, Haigh A, Beerbohm D, (1990) "Continuous slice PENN-PET: a positron tomography with volume imaging capability." Journal of Nuclear Medicine, **31** 617-627

Kinahan P E, Rogers J G, (1989) "Analytic three-dimensional image reconstruction using all detected events." IEEE Transactions in Nuclear Science **NS-36** 964-968

Mumcuoglu E, Leahy R., Cherry S (1996). "Bayesian reconstruction of PET images: methodology and performance analysis." Phys. Med. Biol. **41**: 1777-1807.

Ollinger J.M. (1996). "Model-based scatter correction for fully 3D PET." Phys. Med. Biol. **41**: 153-176.

Russell M, Richards J., Adair T, Wehr J, Richards A (1984). Physics of the Atom, Addison-Wesley.

Shao L., Freifelder R., Karp J.S. (1994). "Triple energy window scatter correction method for PET." IEEE Trans. Med. Imaging **MI-13**: 641-648.

Swain, T. (1998). "Description of Raw PET Data." Private Communication, CTI PET Systems, Inc.

Shepp, L.A., Vardi, Y. (1982). "Maximum likelihood reconstruction for emission tomography." IEEE Trans. Med. Imaging **1**: 113-122.

Woods RP, Cherry S., Mazziotta JC (1992). "Rapid automated algorithm for aligning and reslicing PET images." Journal of Computer Assisted Tomography **16**: 620-633.

Woods RP, Grafton S., Holmes CJ, Cherry SR, Mazziotta JC (1998A). "Automated image registration: I. General methods and intrasubject, intramodality validation." Journal of Computer Assisted Tomography **22**: 141-154.

Woods RP, Grafton S., Watson JDG, Sicotte NL, Mazziotta JC (1998B). "Automated image registration: II. Intersubject validation of linear and nonlinear models." Journal of Computer Assisted Tomography **22**: 155-165.

Woods RP, Mazziotta J., Cherry SR (1993). "MRI-PET registration with automated algorithm." Journal of Computer Assisted Tomography **17**: 536-546.

VITA

Girish Gvalani was born in Calcutta, India on November 26, 1968. He attended Jesuit schools in the parochial system of Calcutta, where he graduated from St. Xavier's High School in May 1987. He entered Davidson College, Davidson, North Carolina, during August of 1988, where in May, 1992 he received the Bachelor of Arts in Physics with Honors. He then entered the graduate program in Medical Physics at Duke University during August 1992, where in May 1995 he received the Master of Science in Medical Physics. He then entered the doctoral program in Solid State Physics at the University of Tennessee during August 1995 but transferred to the Computer Science program during August 1997, where in August 1999 he received his Masters degree.